J. Fluid Mech. (2023), *vol*. 962, A28, doi:10.1017/jfm.2023.292

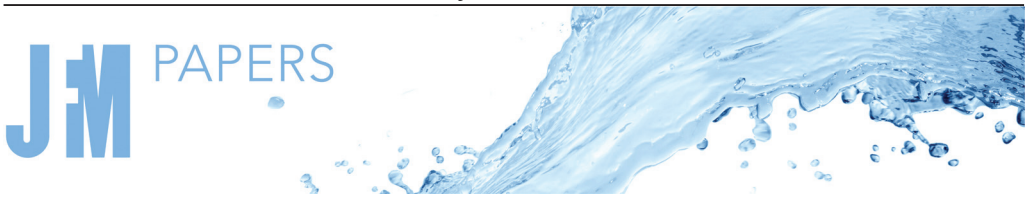

Vertically neutral collapse of a pulsating bubble at the corner of a free surface and a rigid wall

Shi-Min Li[1], **A-Man Zhang**[1,†], **Pu Cui**[1], **Shuai Li**[1] **and Yun-Long Liu**[1]

[1]College of Shipbuilding Engineering, Harbin Engineering University, Harbin 150001, PR China

(Received 19 September 2022; revised 3 March 2023; accepted 3 April 2023)

Vertically neutral collapse of a pulsating bubble occurs when the boundaries above or below the bubble balance the buoyancy effect over a pulsation. In this study, the vertically neutral collapse of a bubble near a vertical rigid wall below the free surface is investigated. The boundary integral method (BIM) is employed to model the bubble dynamics with an open-domain free surface. Moreover, this method is validated against several buoyant bubble experiments. Bubble dynamics in such conditions are associated with three dimensionless parameters: the bubble-free surface distance γ_f, bubble–wall distance γ_w and buoyancy parameter δ. We derive the Kelvin impulse of a spherical bubble and the algebraic relationship for vertically neutral collapse, which proves to be accurate for predicting vertically neutral collapse when the bubble is relatively far from the boundaries. Four patterns of the vertically neutral collapse of the bubble for different γ_w and γ_f are identified: (i) formally downward jet; (ii) annular collapse; (iii) horizontal jet; and (iv) weak jet. Despite the downward jet shape, the 'formally downward jet' is in the vertically neutral collapse state in terms of the profile of toroidal bubbles and the orientation of local high-pressure zones around the bubble at jet impact. A bulge with a high curvature above the bubble in the 'annular collapse' pattern is formed during bubble collapse under two local high-pressure zones at the left and right extremities of the bubble. The 'horizontal jet' pattern has the greatest potential to attack the wall, and the power laws of the moment of the jet impact, jet velocity and bubble displacement with respect to the theoretical Kelvin impulse are discussed. In particular, we quantitatively illustrate the role of the free surface on bubble migration towards the wall through the variational power-law exponents of the bubble displacement with respect to γ_w.

Key words: bubble dynamics

† Email address for correspondence: zhangaman@hrbeu.edu.cn

1. Introduction

Large-scale pulsating bubbles are affected by two opposite pressure gradients near the free surface, including the upward pressure gradient from the free surface and the downward hydrostatic pressure gradient, which are closely related to underwater explosions (Klaseboer *et al.* 2005*a*; Song *et al.* 2017; Javier *et al.* 2021; Nguyen *et al.* 2021), air-gun exploration (Ziolkowski *et al.* 1982; Babak & Martin 2018; Khodabandeloo & Landro 2018; Ziolkowski 2021) and submarine volcanic eruptions (Lyons *et al.* 2019; Mendoza, Clemente & Hernandez 2020). In some cases, the upward buoyancy essentially balances the effect of the free surface, causing the bubble to bear no upward or downward momentum at the end of bubble collapse, which is called 'vertically neutral collapse' in this study. The bubble has no migration trend in the vertical direction in the 'vertically neutral collapse' state, and similar features also occur when a buoyant bubble is near the rigid bottom (Brujan, Pearson & Blake 2005), when a cavity is near the composite surfaces (Shima *et al.* 1989) or in a liquid gap (Gonzalez-Avila *et al.* 2011). When the vertically neutral collapse occurs, the bubble behaviour is more complicated than those cases when a Bjerknes force from any boundary dominates (Blake, Taib & Doherty 1986, 1987). An in-depth understanding of the vertically neutral collapse of bubbles, such as bubble morphology and jet direction, can help to rationalize the use of explosives or air-guns and prevent disasters caused by buoyant bubbles.

Bubble dynamics in the vicinity of a single free surface have been extensively studied in previous works. When the buoyancy effect is weak, the generation of a downward liquid jet is the most essential feature of the bubble (Chahine 1977; Blake 1981; Tomita, Kodama & Shima 1991; Li *et al.* 2019*b*; Saade *et al.* 2021; Zhang *et al.* 2023*a*). As the buoyancy increases, the influence of the free surface on the downward bubble migration is counteracted to varying degrees, resulting in vertically neutral collapses or upward liquid jets (Blake *et al.* 1987; Wang *et al.* 1996*a*,*b*; Zhang *et al.* 2015; Li, Zhang & Liu 2021; Liu *et al.* 2023). However, in practical cases, other boundaries, such as the seacoast or structures, often exist in the neighbourhood of the bubble below the free surface. As vertically neutral collapse occurs, the bubble undergoes no obvious upward or downward migration. Thus, the bubble migrates only towards the surrounding structure, damaging the structure directly (Lechner *et al.* 2017, 2019; Tian *et al.* 2020) or by transferring energy to suspended solids in water (Borkent *et al.* 2008; Wu *et al.* 2017; Zhang *et al.* 2019). However, it is difficult to determine the direction and intensity of bubble migration due to the complicated behaviour of the bubble as vertically neutral collapse occurs, which is a motivation of this study.

Previous studies on the interaction between the bubble and nearby structures below the free surface have paid more attention to the physical phenomena in some specific engineering scenarios, such as the rise and fall of the free surface (Liu *et al.* 2016; Zhang *et al.* 2017), interaction between the bubble and a vessel (Klaseboer, Khoo & Hung 2005*b*; Zhang & Zong 2011; Zhang, Zong & Zhang 2014), and deformation of the floating structure caused by bubble pulsations (Klaseboer *et al.* 2005*a*; Zong *et al.* 2015). Some parametric analysis of the bubble collapse has been conducted: Kiyama *et al.* (2021) and Tagawa & Peters (2018) used the method of images to develop a theoretical model for determining the jet direction when a cavity is near a corner; Molefe & Peters (2019) studied the jet direction when a cavity is within rectangular and triangular channels; Andrews, Rivas & Peters (2020) predicted the jet direction near a slot with the boundary integral method (BIM); and Brujan conducted comprehensive studies on the corner of two or three rigid boundaries (Brujan *et al.* 2018; Brujan, Hiroyuki & Toshiyuki 2019; Brujan *et al.* 2022). These parametric studies provide references for quantifying the collapse

characteristics of bubbles, but no buoyant bubbles are involved in their works. However, the strong buoyancy effect for large-scale bubbles would change the collapse characteristics of bubbles significantly. In our previous studies (Li *et al.* 2019*a*), the jet characteristics are investigated for typical buoyancy effects when the bubble is initiated near a free surface and two crossed walls. However, as a special case, a theoretical criterion for the occurrence of vertically neutral collapse and quantitative analysis of bubble dynamics are worthy of further study, which will help to enhance the understanding of bubble dynamics in the entire buoyancy-distance parameter domain and better control the effects of bubble collapse. In general, systematic research on the dynamics of bubbles with obvious buoyancy near the free surface and structures was rare in previous studies, which is an important purpose behind this study.

In this study, we combine theoretical and numerical methods to study the vertically neutral collapse of a pulsating bubble at the corner of the free surface and a semi-infinite vertical rigid wall, which is the most fundamental physical scene for bubble dynamics affected by nearby structures below the free surface. An in-depth understanding of the physical mechanisms for such basic boundary conditions can provide a foundation for solving more complex problems in the future. First, the occurrence condition for vertically neutral collapses is one of the difficult issues. Kelvin impulse theory provides a valuable way to link the buoyancy of the bubble and the distances to boundaries. The Kelvin impulse, which is the time integral of the force acting on the bubble surface, was used by Blake *et al.* (1986, 1987) to determine the jet direction of a buoyant bubble near a single wall or free surface. A quantitative relationship between the buoyancy and the distance parameters (we call it the 'Blake criterion') is given in his works. Brujan *et al.* (2005) also concluded that the Kelvin impulse can reflect the jet pattern and orientation near a rigid wall, and other applications, including the inertial boundary and two-fluid interface, were also well developed (Blake, Leppinen & Wang 2015; Han *et al.* 2022). Based on their ideas that we combine with the method of the mirror source/sink, we deduce and develop the quantitative relationship among the buoyancy, the bubble-free surface distance and the bubble–wall distance when vertically neutral collapse occurs.

Regarding the numerical method, the BIM has been widely applied in modelling bubble dynamics because of its high accuracy and efficiency in dealing with the three-dimensional problem (Shima & Sato 1980; Wang & Blake 2010, 2011; Zhang & Liu 2015; Li *et al.* 2021; Zhang *et al.* 2023*b*). Therefore, BIM is adopted to simulate the behaviour of the bubble and free surface, with the rigid wall equivalent to the mirror bubble and free surface. The free surface is processed as an open plane instead of a closed area to improve the computational accuracy and efficiency. The numerical codes are validated against several buoyant bubble experiments.

Finally, a comprehensive study on the vertically neutral collapse characteristics over a large parametric range (except for those cases where the bubble contacts boundaries) is carried out. Four collapse patterns of the bubble are performed based on the distance to boundaries, i.e. 'formally downward jet', 'annular collapse', 'horizontal jet' and 'weak jet'. Among them, in the 'horizontal jet' pattern, the bubble only migrates towards the rigid wall, and this pattern occupies most of the parameter domain of interest. Therefore, we conduct parametric research on the essential features, including the moment of the jet impact, jet velocity and bubble displacement. Compared with the situation in which a cavity is near a single rigid wall (Supponen *et al.* 2016), the power laws of the three characteristic parameters with the theoretical Kelvin impulse are found and summarized.

The structure of this paper is as follows. We first present the numerical method in § 2 and define the standard of the vertically neutral collapse in § 3. The theoretical conditions

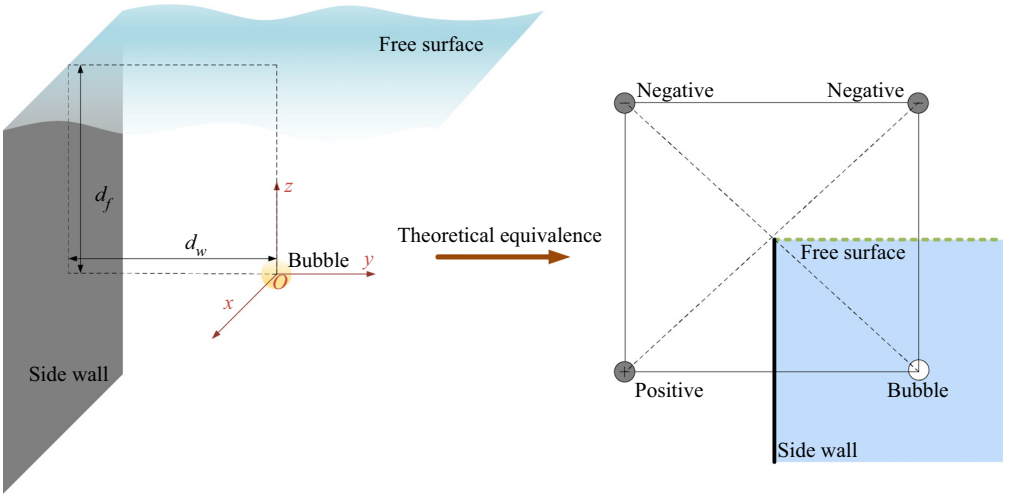

Figure 1. Schematic of the physical model.

for the vertically neutral collapse of a spherical bubble are derived using Kelvin impulse theory in § 4. Moreover, several mechanistic experiments are used to verify the numerical algorithm in § 5. Then, we discuss the applicability of Kevin impulse theory in § 6. Four typical features for vertically neutral bubble collapse are illustrated in § 7. Finally, we carry out the parameter analysis on the most important feature ('horizontal jet') in § 8 and summarize the work in § 9.

2. Physical model

2.1. *Parameter definition*

The schematic representation of the physical model is illustrated in figure 1. The origin is taken at the centre of the initial bubble, with the y-axis horizontally to the right and the z-axis vertically upward. The vertical rigid wall intersects the free surface in the negative y-axis direction, as shown in the left half of figure 1. Two distance parameters are studied: the bubble-free surface distance d_f and bubble–wall distance d_w. In subsequent theoretical derivations, three singularities are adopted to include the influence of the free surface and sidewall, as shown in the right half of figure 1. The positive circle denotes the same source/sink strength as the bubble, and the negative circles indicate the converse strength.

2.2. *Numerical implements*

To obtain the general results, all physical quantities are dimensionless unless otherwise specified. The bubble radius at the maximum volume R_m is taken as the reference length, with the density of the liquid ρ as the reference density and the hydrostatic pressure at the origin P_a as the reference pressure. We first provide the three most important dimensionless parameters, namely, the bubble-free surface distance γ_f, the bubble–wall distance γ_w and the buoyancy parameter δ:

$$\gamma_f = \frac{d_f}{R_m}, \quad \gamma_w = \frac{d_w}{R_m}, \quad \delta = \sqrt{\frac{\rho g R_m}{P_a}}. \tag{2.1a–c}$$

The bubble pulsation in this study is a transient process that begins with an initial small high-pressure bubble. The flow field can be reasonably regarded as inviscid, irrotational and incompressible (Blake & Gibson 1987; Wang & Blake 2010). Therefore, the potential flow theory is adopted to control the fluid domain and the fluid velocity potential satisfies the Laplace equation:

$$\nabla^2\varphi = 0, \tag{2.2}$$

where φ represents the dimensionless velocity potential with the reference quantity of $R_m\sqrt{P_a/\rho}$.

Equation (2.2) can be transformed into the boundary integral equation (Wang 2013; Wang, Kawa & Michael 2015) by Green's three theorems:

$$\lambda\varphi = \oint_s \left(G_r\frac{\partial\varphi}{\partial n} - \varphi\frac{\partial G_r}{\partial n}\right)\mathrm{d}s, \tag{2.3}$$

where λ is the solid angle, s is the surface of all boundaries and G_r is the Green function ($G_r = 1/|\boldsymbol{p}-\boldsymbol{q}|$; $\boldsymbol{p}$ is the field point and $\boldsymbol{q}$ is the integral point).

The dynamic boundary conditions (Chahine *et al.* 2016; Gong *et al.* 2018) for the bubble surface and the free surface are determined by the Bernoulli equation:

$$\frac{\mathrm{d}\varphi}{\mathrm{d}t} = 1 - \varepsilon\left(\frac{V_o}{V}\right)^{\kappa} + \frac{1}{2}|\nabla\varphi|^2 - \delta^2 z \tag{2.4}$$

$$\frac{\mathrm{d}\varphi}{\mathrm{d}t} = \frac{1}{2}|\nabla\varphi|^2 - \delta^2(z-\gamma_f), \tag{2.5}$$

where ε is the strength parameter denoting the dimensionless initial inner pressure of the bubble; V_o and V are the bubble volumes at the initial and present moment, respectively; and κ is the ratio of specific heats.

The boundary consists of three parts: the bubble surface, the free surface and the rigid sidewall. The rigid wall can be included by the influence of the symmetrical bubble and free surface about the wall. The boundary integral equation is ultimately discretized into a matrix form: $G_{ij}\partial\varphi_j/\partial n_j = H_{ij}\varphi_j$. The calculation method of G_{ij} and H_{ij} and the implementation of the matrix can be found in the previous literature (Wang *et al.* 2015). Notably, two bubbles and an infinite free surface, including the real and mirrored nodes, are considered in the matrix here.

Since (2.3) requires the computed boundaries to form a closed surface, additional nodes must be discretized above the free surface, reducing the computational efficiency and accuracy. In this study, the influence of additional nodes is included by the induced velocity potential of a virtual vortex based on the equivalence of a vortex ring and the distributed dipole (Zhang *et al.* 2001). The virtual vortex ring consists of the outermost circle of the meshed free surface. The scale of the free surface established in numerical simulations is 15 times R_m to reduce the error caused by the influence of the far-field free surface to less than 1 % (Liu *et al.* 2016). Here, we provide a modified expression for the diagonal elements of the matrix H:

$$H_{ii} = -\sum_{\substack{j=1,n\\ j\neq i}} H_{ij} - \frac{1}{4\pi}\oint_{C_1+C_2}\left(\frac{r_z}{\sqrt{{r_x}^2+{r_y}^2+{r_z}^2}} - 1\right)\frac{\mathrm{d}l_x\cdot r_y - \mathrm{d}l_y\cdot r_x}{{r_x}^2+{r_y}^2} - 1, \tag{2.6}$$

where i and j are the node numbers; $C_1 + C_2$ is the virtual vortex consisting of the outermost circle of the real and mirrored free surface; $\boldsymbol{r}$ is the vector from the virtual

vortex ring to the nodes on the boundary; taking the normal direction of the virtual vortex as the z direction, r_x, r_y and r_z are the three components of $\boldsymbol{r}$ in the local coordinate system; and $\mathrm{d}\boldsymbol{l}$ is the element vector of the virtual vortex with the two tangential components of $\mathrm{d}l_x$ and $\mathrm{d}l_y$.

Finally, we merge the symmetrical parts of matrices G and H with the rigid wall according to the image method. In this way, the matrix dimension can be reduced by half when the matrix G is inverted.

2.3. *Vortex model*

In some cases, the bubble becomes a ring-shaped bubble due to the collision of the bubble walls, and the velocity potential of the bubble surface is no longer a single-valued function. A 3D vortex model is used to address this problem by adding a vortex ring inside the bubble, which has been fully developed in bubble dynamics (Wang & Blake 2011; Li *et al.* 2016). Then, φ is decomposed into the induced velocity potential φ_v and the residual velocity potential φ_r:

$$\varphi = \varphi_v + \varphi_r. \tag{2.7}$$

The residual velocity potential φ_r can be updated according to the process in § 2.2, while the induced velocity u_v and velocity potential φ_v need to be calculated by Biot–Savart's law and a semi-analytic method (Zhang & Liu 2015), respectively:

$$u_v = \frac{K}{4\pi} \oint\limits_{C_1'+C_2'} \frac{\boldsymbol{r} \times \mathrm{d}\boldsymbol{l}}{|\boldsymbol{r}|^3}, \tag{2.8}$$

$$\varphi_v = \frac{K}{4\pi} \oint\limits_{C_1'+C_2'} \left(\frac{r_z}{\sqrt{{r_x}^2 + {r_y}^2 + {r_z}^2}} \pm 1 \right) \frac{\mathrm{d}l_x \cdot r_y - \mathrm{d}l_y \cdot r_x}{{r_x}^2 + {r_y}^2}, \tag{2.9}$$

where K is the jump of the velocity potential on the impacted nodes; the definitions of $\boldsymbol{r}$ and $\mathrm{d}\boldsymbol{l}$ are the same as those in (2.6) with the normal direction of the vortex inside the bubble as the z direction; C_1' and C_2' denote the vortex ring inside the bubble and its mirror with the sidewall, respectively; and '$\pm$' depends on the position of nodes in which '$+$' is adopted when the nodes are underneath the vortex and '$-$' is employed otherwise.

3. Definition of vertically neutral collapse

In this study, the vertically neutral collapse of a bubble means that the vertical momentum of the bubble is zero at the end of collapse; that is, the bubble has no tendency to continue migrating vertically after the first cycle of pulsation. Since the migration velocity of the bubble is zero, the momentum of the bubble can be calculated by the Kelvin impulse (Blake *et al.* 1986, 1987), which is the time integral of the 'forces' acted upon by the buoyancy and boundaries:

$$\boldsymbol{I}_b = \oint\limits_{s_b} \varphi \boldsymbol{n} \, \mathrm{d}s, \tag{3.1}$$

where s_b and $\boldsymbol{n}$ are the bubble surface and its unit normal vector, respectively.

In BIM simulations, the bubble undergoes large deformation, resulting in an uneven distribution of the velocity potential on the bubble surface. The Kelvin impulse of the bubble can be obtained by integrating the velocity potential of the bubble surface through

(3.1). In this study, we define the Kelvin impulse of the bubble in numerical simulations as $\boldsymbol{I}_s$:

$$\boldsymbol{I}_s = \sum_{i=1}^{m} \varphi_i s_i \boldsymbol{n}_i, \tag{3.2}$$

where m is the number of elements on the bubble surface; and φ_i, s_i and n_i denote the velocity potential, area and unit normal vector of element i, respectively.

Here, $\boldsymbol{I}_s$ is used to reflect the momentum of the deformable bubble in the simulations. Thus, $I_{sz} = 0$ (I_{sz} denotes the component along the z axis) at the end of bubble collapse is the standard to determine the vertically neutral collapse state.

4. Kelvin impulse theory based on the assumption of spherical bubbles

When we ignore the deformation of the bubble and regard it as a time-varying point source or sink, the expression of the above equation under different boundary conditions can be solved theoretically. For example, two equal-intensity point sources are equivalent to an infinite rigid wall on their perpendiculars, and one point source plus one equal-intensity sink are equivalent to a free surface without fluctuations. The velocity potential produced by a point source with an intensity of $m(t)$ and at a point (x_0, y_0, z_0) is

$$\varphi = -\frac{m\,(t)}{4\pi\sqrt{(x-x_0)^2 + (y-y_0)^2 + (z-z_0)^2}}. \tag{4.1}$$

Since the bubble is regarded as a point source, the influence of the boundary can be equivalent to one point source symmetric to the rigid wall and two sinks symmetric to the free surface, as shown in figure 1. Thus, the induced velocity φ at the bubble can be written as

$$\nabla\varphi = -\frac{m\,(t)}{4\pi}\left(-\frac{1}{(2\gamma_w)^2}\boldsymbol{y} + \frac{1}{(2\gamma_f)^2}\boldsymbol{z} + \frac{1}{\left(2\sqrt{\gamma_w^2+\gamma_f^2}\right)^2}\frac{-\gamma_w\boldsymbol{y}+\gamma_f\boldsymbol{z}}{\sqrt{\gamma_w^2+\gamma_f^2}}\right). \tag{4.2}$$

The Kelvin impulse of the bubble caused by the boundaries (Best & Blake 1994) can be obtained from

$$I = \int_0^t -m(t)\nabla\varphi\,\mathrm{d}t, \tag{4.3}$$

where the source intensity $m(t)$ is calculated by the pulsation velocity of the Rayleigh bubble (Blake *et al.* 1987; Rayleigh 1917) with the constant inner bubble pressure of saturated vapour pressure:

$$m\,(t) = 4\pi R^2\sqrt{\frac{2}{3}\left(\frac{1}{R^3}-1\right)}. \tag{4.4}$$

Taking into account the buoyancy effect, the Kelvin impulse is transformed into

$$I = \oint_{s'} \left(-m(t)\nabla\varphi + \delta^2 \boldsymbol{z}\right) \mathrm{d}s'$$
$$= \frac{1}{4\pi}\left(-\frac{1}{(2\gamma_w)^2}\boldsymbol{y} + \frac{1}{(2\gamma_f)^2}\boldsymbol{z} + \frac{1}{\left(2\sqrt{\gamma_w^2+\gamma_f^2}\right)^2}\frac{-\gamma_w \boldsymbol{y} + \gamma_f \boldsymbol{z}}{\sqrt{\gamma_w^2+\gamma_f^2}} + \delta^2 \boldsymbol{z}\right)\int_0^t m^2(t)\,\mathrm{d}t. \tag{4.5}$$

Simplifying the above formula, the value of the Kelvin impulse components ($t = 1.83$) in the horizontal and vertical directions can be obtained:

$$I_y = \frac{2\sqrt{6}\pi}{9}\left[\left(\frac{1}{\gamma_w^2} - \frac{1}{\gamma_w^2+\gamma_f^2}\frac{\gamma_w}{\sqrt{\gamma_w^2+\gamma_f^2}}\right)\right] B\left(\frac{7}{6},\frac{3}{2}\right), \tag{4.6}$$

$$I_z = \frac{2\sqrt{6}\pi}{9}\left[\left(\frac{1}{\gamma_f^2} + \frac{1}{\gamma_w^2+\gamma_f^2}\frac{\gamma_f}{\sqrt{\gamma_w^2+\gamma_f^2}}\right) B\left(\frac{7}{6},\frac{3}{2}\right) - 2\delta^2 B\left(\frac{11}{6},\frac{1}{2}\right)\right], \tag{4.7}$$

where $\boldsymbol{B}$ is the beta function.

We let I_z be zero, and we obtain the algebraic relationship for vertically neutral collapse of a spherical bubble (the process can be seen in Appendix A):

$$\gamma_f \delta = 0.442\sqrt{1+\sin^3\left(\arctan\left(\frac{\gamma_f}{\gamma_w}\right)\right)}. \tag{4.8}$$

When the vertical wall does not exist, the above formula degenerates into the classical 'Blake criterion' ($\gamma_w \to \infty$) for determining the direction of the bubble jet in the vicinity of the single free surface:

$$\gamma_f \delta = 0.442. \tag{4.9}$$

5. Comparison between the numerical and experimental results

To validate the numerical procedure used in this paper, three buoyant bubble experiments are compared with the computed bubble dynamics. First, two sets of underwater explosions are conducted in a 4 m × 4 m × 4 m steel water tank, and a detailed introduction of the experimental site and devices can be found in the works of Liu *et al.* (2021). Combined with the idea of the image method, we place two explosives with the same equivalence horizontally to include the influence of the vertical rigid wall.

In the first case, 4 g Hexokin explosives generate a pulsating bubble with R_m of 26 cm. The two explosive charges are 70 cm apart and initially 40 cm below the free surface. Thus, the dimensionless distance and buoyancy parameters can be obtained: $\gamma_w = 1.35$, $\gamma_f = 1.54$ and $\delta = 0.16$. We estimate the initial bubble radius R_0 in the numerical simulation by the traditional Rayleigh–Plesset equation (Plesset & Prosperetti 1977), and an arbitrary choice in a reasonable range can be made for the initial strength parameter (120 in this study) because the numerical results are almost the same when it is set from 100 to 500 in dimensionless form (Turangan *et al.* 2006). The adiabatic coefficient κ is taken as 1.22 to match the experimental bubble period since a small difference in the bubble period

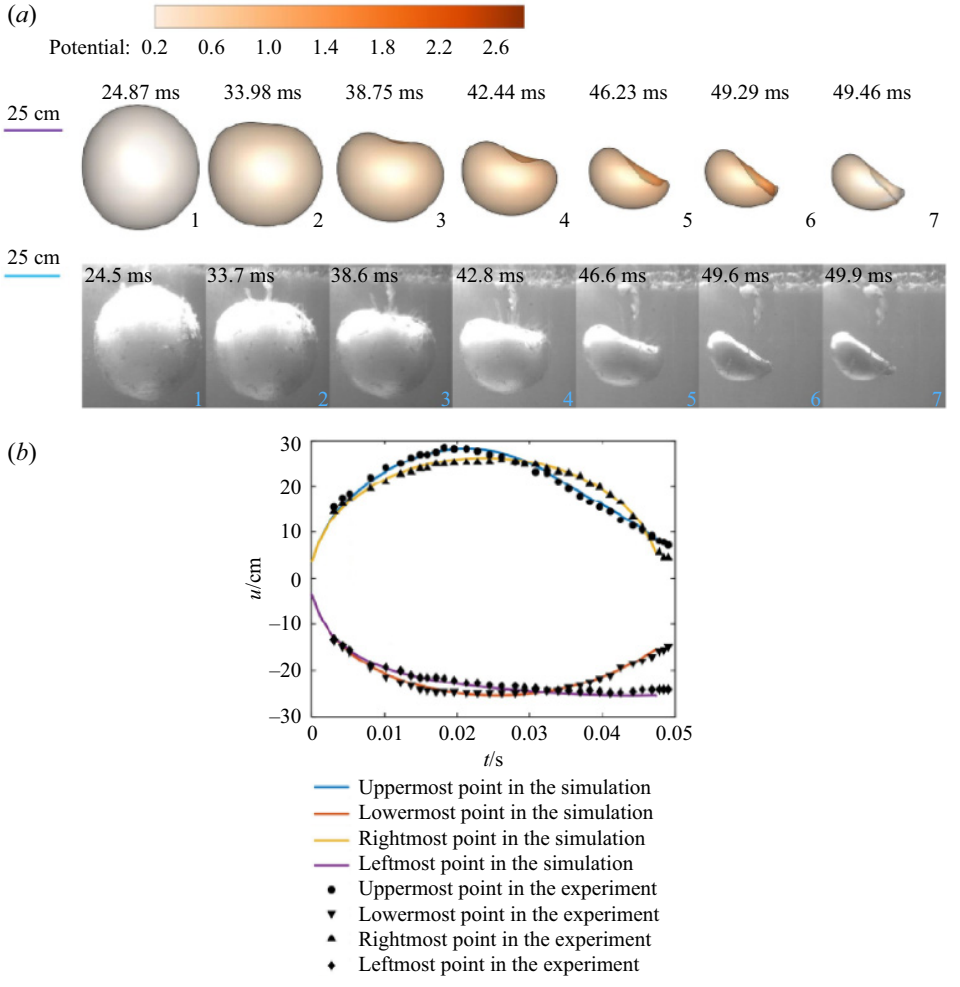

Figure 2. Experimental and numerical bubble dynamics of an underwater explosion bubble for $\gamma_w = 1.35$, $\gamma_f = 1.54$ and $\delta = 0.16$. (*a*) Comparison of the bubble profile at typical moments: the first row is the numerical results, and the colour of the bubble surface represents the velocity potential; the second row is the experimental results shot by a high-speed camera at a frame rate of 10 000 frames s^{-1}; the frame number of each image is marked in the lower right corner, and the corresponding moment is marked in the upper left corner; the ruler of the pictures is drawn on the far left. (*b*) Comparison of the displacement curves of the uppermost, lowermost, rightmost and leftmost points of the bubble.

can be found when κ is in the range from 1.1 to 1.4 (Li *et al.* 2016). Figure 2(*a*) shows a comparison of the bubble profile between the simulation and the experiment at typical moments during bubble collapse. The bubble is almost spherical during the expansion stage and thus not shown. Figure 2 shows the bubble profiles on the right, which indicates that a vertical rigid wall exists 35 cm from the initial bubble on the left. When the bubble expands to the maximum volume (the first frame), the bubble surface near the wall is slightly flattened. Subsequently, the upper bubble surface collapses downward at a larger velocity, forming an oblique downward liquid jet under the combined action of the free surface and the rigid wall (Frames 2–4). The bubble surface farther away from the rigid wall continuously collapses towards the wall (Frames 5 and 6). Finally, the liquid jet impacts the bubble surface to form a ring-shaped bubble (Frame 7). The numerical results

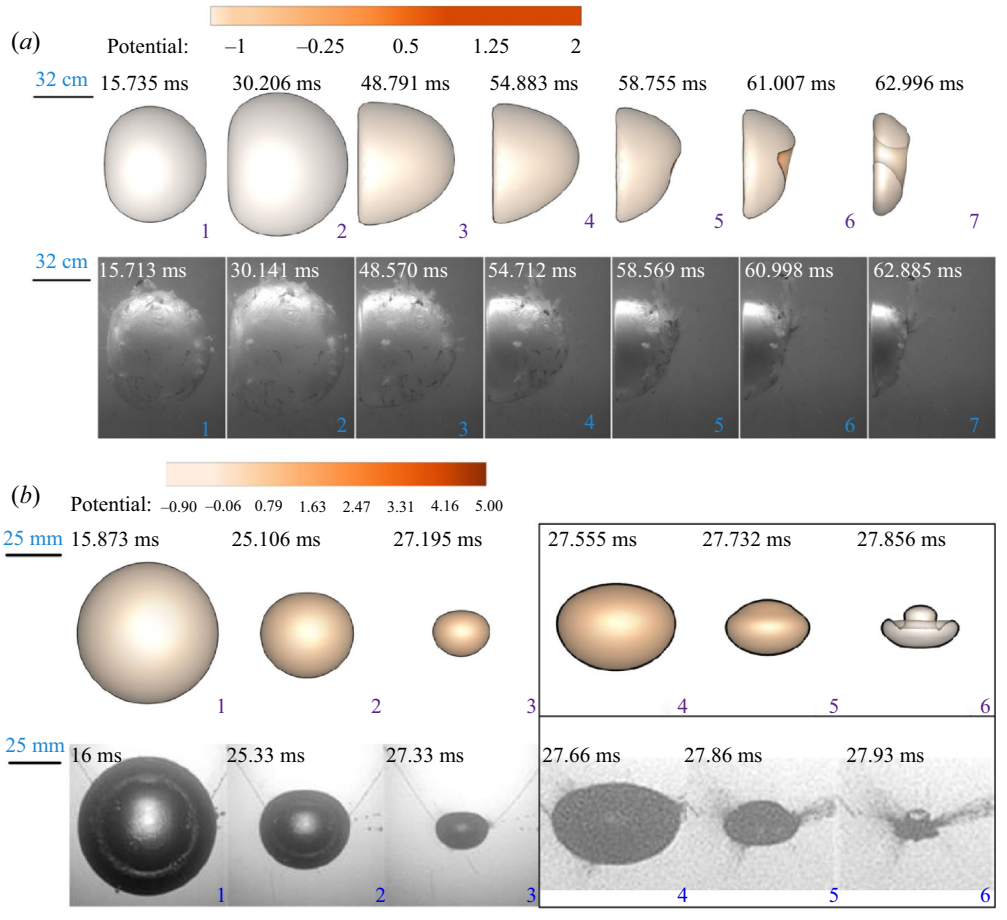

Figure 3. Comparison of the bubble profile in simulations with two typical buoyant bubble experiments. (*a*) An underwater explosion experiment for $\gamma_w = 0.75$, $\gamma_f = 5.62$ and $\delta = 0.17$. (*b*) A buoyant bubble near a single free surface in a decompression tank for $\gamma_f = 1.74$ and $\delta = 0.248$ from the works of Zhang *et al.* (2015). The ruler of the first three frames is drawn on the far left, and the three frames inside the black box are the enlarged view to visualize more details.

reproduce the experimental phenomena well. To quantitatively validate the numerical results, we compare the displacements of the uppermost, lowermost, rightmost and leftmost points of the bubble surface with the experimental measurements, as shown in figure 2(*b*). The bubble displacement in the numerical simulation agrees well with the experimental measurements, with slight differences originating from measurement errors or the numerical smoothing techniques.

Next, we compare the other two buoyant bubble experiments with the computed bubble profiles because of the similar dynamic characteristics to the case of vertically neutral collapse, as shown in figure 3. The first case is the underwater explosion bubble, and the experimental system is the same as that in figure 2, as shown in figure 3(*a*). Two Hexokin explosives at a distance of 53 cm with a charge of 10 g are detonated at a depth of 1.8 m, producing two bubbles with a maximum radius of 35 cm. This is equivalent to a rigid wall placed 26.5 cm horizontally away from the bubbles. The dimensionless distance and buoyancy parameters are $\gamma_w = 0.75$, $\gamma_f = 5.62$ and $\delta = 0.17$. The dimensionless initial conditions of the bubble in the BIM model are the same as those in figure 2. During

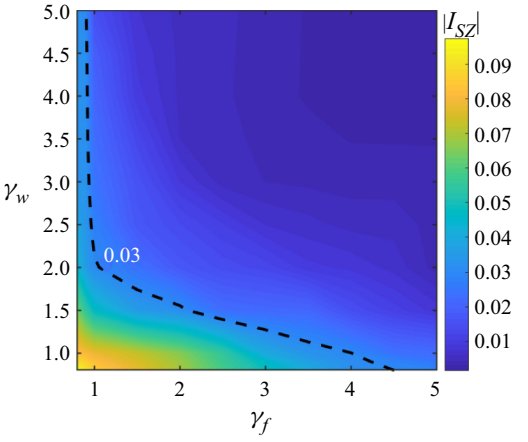

Figure 4. Distribution of errors for Kelvin impulse theory. The black dashed line indicates an error contour of 0.03.

bubble expansion, the left side of the bubble is flattened by the equivalent rigid wall. An obliquely upward liquid jet is generated due to the weak effect of the free surface, which agrees with the computed bubble dynamics very well. If the explosive charge could be adjusted precisely to the case in which the buoyancy effect is exactly offset by the free surface, the bubble would reach the vertically neutral collapse state and the liquid jet would be directed horizontally.

Figure 3(*b*) presents a spark-induced bubble near the single free surface with a stronger buoyancy effect ($\delta = 0.248$). The experimental image is obtained from Zhang *et al.* (2015) by reducing the pressure of air to increase the buoyancy of bubbles. The initial dimensionless distance of the bubble from the free surface γ_f is 1.74. The computed initial conditions of the bubble are set to $\varepsilon = 100$ and $\kappa = 1.4$. The upper side of the bubble is first flattened under the action of the free surface, and subsequently, the left and right sides of the bubble sag inward. At the end of bubble collapse, an annular jet is formed accompanied by a bulge above the bubble. In this case, the bubble does not show obvious upward or downward migration, which is very close to the case of vertically neutral collapse. The computed bubble dynamics are compared with the experimental images at typical moments in which good agreement is achieved. Notably, the bubble in the numerical simulation is larger than the sparked-induced bubble near the minimum bubble volume (the last frame). The most likely reason for the visible discrepancies is the lack of the effect of non-equilibrium evaporation and condensation on the bubble surface in the numerical procedure. However, in general, the BIM simulation reproduces the main features of jet formation and development well.

6. Condition and error of vertically neutral collapse

The condition of vertically neutral collapse is associated with δ, γ_f and γ_w. It is expected that the condition for a spherical bubble (4.8) can be applicable with acceptable errors when the bubble is relatively far from the boundaries. According to the definition of vertically neutral collapse in § 3, the absolute value of I_{sz} at jet impact is regarded as the error (in a few cases, when the jet is too weak to impact the bubble surface, I_{sz} at the moment of the minimum bubble volume is taken as the error). To clarify the condition and error of vertically neutral collapse, we use the buoyancy parameter δ calculated by

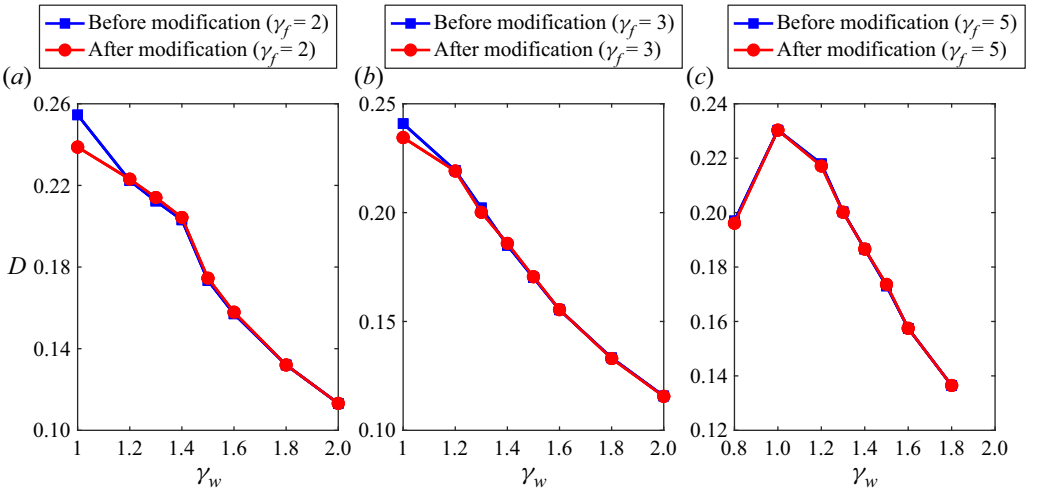

Figure 5. Comparison of the bubble displacement before and after modification for different γ_f and γ_w. The results before modification are simulated directly using (4.8); the results after modification are corrected by adjusting δ until $|I_{sz}|$ is less than 0.01.

(4.8) to model the bubble behaviour for various γ_f and γ_w in BIM simulations. Figure 4 shows the distribution of the errors for different γ_f and γ_w. The value of the error decreases as the bubble moves away from the boundaries because the bubble is closer to spherical oscillation if it is less affected by the boundaries. A contour line with a magnitude of 3 % is plotted, as shown by the black dashed line in figure 4. Areas with an error higher than 3 % are mainly concentrated near the corner of the free surface and the rigid wall.

In this study, we use the value of 3 % as an acceptable threshold of errors, which is attributed to the influence of the error on the characteristic parameters of the bubble. Figure 5 illustrates the variation of the bubble displacement D with γ_w for three typical γ_f values ($\gamma_f = 2$, 3 and 5), in which the blue line represents the result under the δ calculated using (4.8), and the result of the red line modifies (4.8) to make $|I_{sz}|$ drop below 0.01 by adjusting δ. When $\gamma_f = 2$, a visible difference between the bubble displacement D before and after modification occurs when γ_w is less than approximately 1.5; when $\gamma_f = 3$, the visible difference occurs when γ_w is less than 1.3; and when $\gamma_f = 5$, the bubble displacement before and after modification is almost the same. In these examples, the γ_f and γ_w corresponding to significant changes in the bubble displacement before and after modification almost fall on the contour line of 0.03 in figure 5. Therefore, in subsequent investigations, we adjust δ to reduce I_{sz} below 0.03 to make the bubble reach a vertically neutral collapse state when $|I_{sz}|$ is greater than 0.03. In conclusion, (4.8) can accurately predict the vertically neutral collapse of the bubble when the error is within 0.03. If the bubble is near the boundaries when the error exceeds 0.03, δ needs to be obtained separately for the fixed γ_f and γ_w to match the vertically neutral collapse, and specific values of δ for different γ_f and γ_w are given in a later section.

7. Results

Four typical collapse patterns are discussed in terms of the bubble behaviour, bubble migration and Kelvin impulse to gain a qualitative understanding of the vertically neutral collapse behaviour of bubbles. The dimensionless computed initial conditions of the bubble are set as $R_0 = 0.14$, $\varepsilon = 120$ and $\kappa = 1.25$.

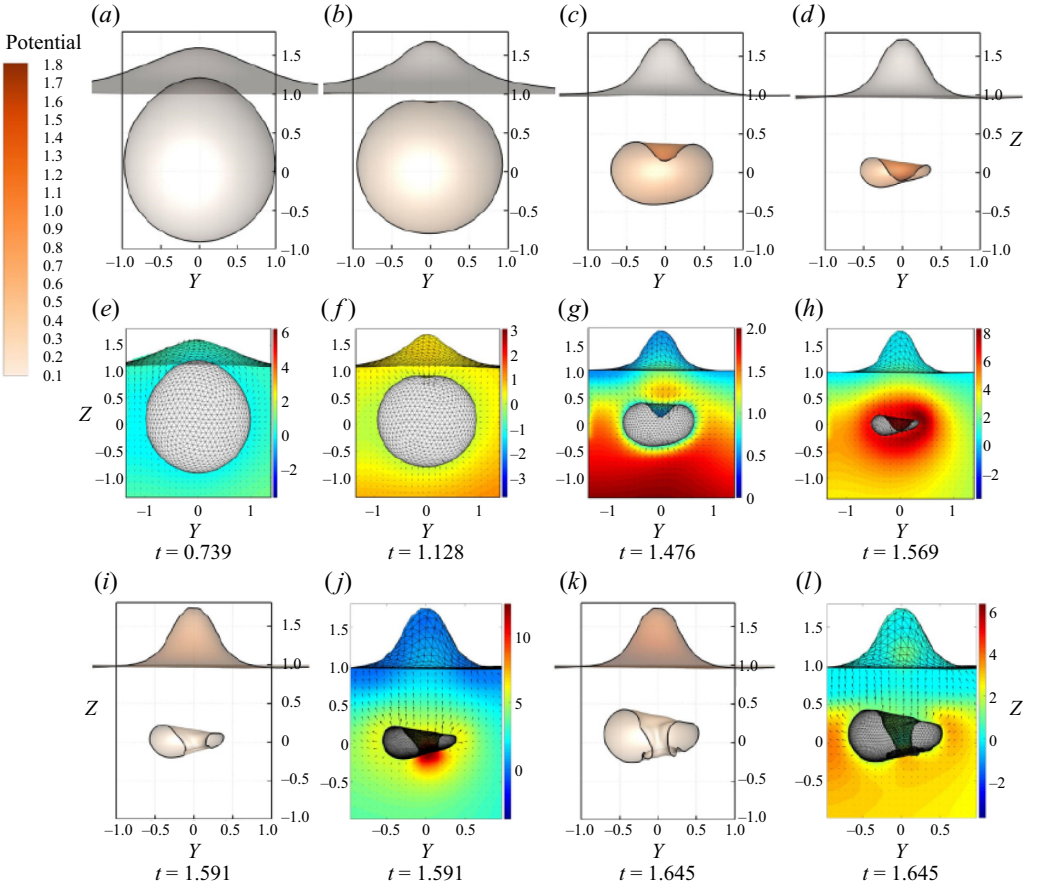

Figure 6. Bubble behaviour and surrounding pressure distribution at the collapse stage for $\gamma_f = 1$, $\gamma_w = 2$ and $\delta = 0.461$.

7.1. *Formally downward jet*

In the first case, the bubble initiated close to the free surface is considered for $\gamma_f = 1$ and $\gamma_w = 2$. The bubble behaviour, the surrounding pressure and velocity field at typical moments are provided, as shown in figure 6. The bubble remains almost spherical for most of the expansion process. However, the free surface sinks the upper part of the bubble near the maximum bubble volume, so we show only the collapse process of the bubble. After the bubble reaches the maximum volume (the first frame), the free surface directly above the bubble is significantly raised. The upper part of the bubble is flattened, producing a downward liquid jet. This downward liquid jet results from the conserved momentum of the flow field and a local high-pressure zone between the bubble and free surface, as shown at $t = 1.476$, which is observed and clarified in many works related to bubble-free surface interaction (Wang *et al.* 1996*a*; Zhang *et al.* 2017; Li *et al.* 2019*b*). After $t = 1.569$, the liquid jet impacts the lower bubble surface, and then the flow field becomes a double-connected region. Subsequently, the bubble rebounds with an annular shape. As seen from the last two frames, the lower part of the bubble produces an upwardly developing protrusion during the rebounding stage instead of developing downward. Although the jet direction is downward in the first cycle, the bubble exhibits

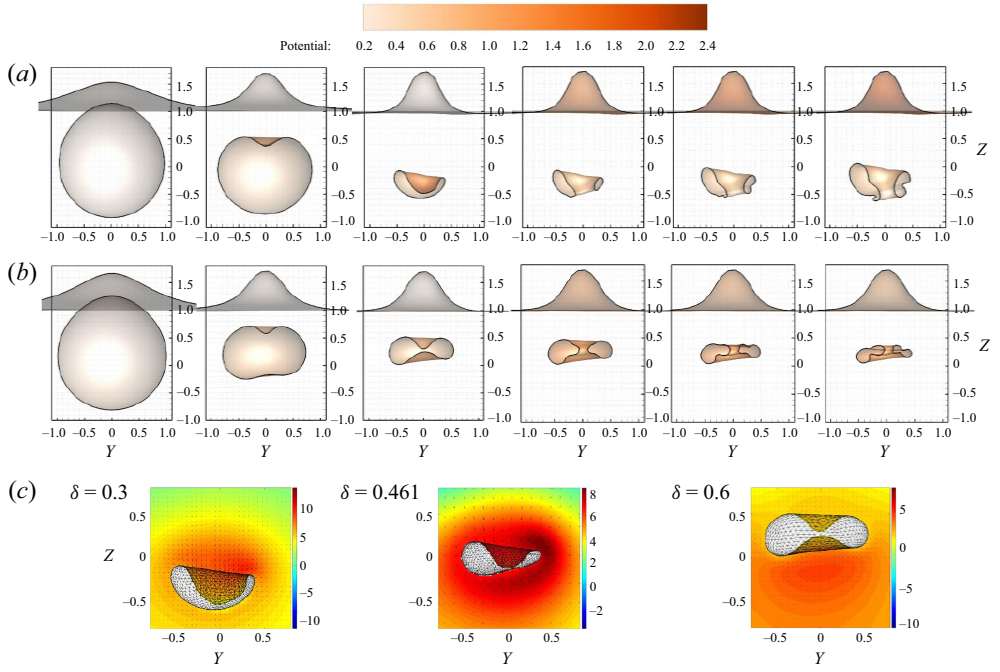

Figure 7. Comparison of bubble behaviours for different buoyancy parameters. Temporal development of the bubble shape for (*a*) $\delta = 0.3$, (*b*) $\delta = 0.6$; (*c*) the pressure distribution surrounding the bubble at jet impact for three δ.

no evident downward migration during the rebounding stage due to the buoyancy effect. We call this collapse pattern the 'formally downward jet'.

Interestingly, the 'formally downward jet' concept seems to challenge the premise of the 'vertically neutral collapse' state in terms of the jet morphology. To validate that the 'formally downward jet' is indeed in the 'vertically neutral collapse' state, figure 7 compares the bubble profile for three different buoyancy parameters ($\delta = 0.3, 0.461, 0.6$), under which the jetting behaviour of the bubble can be easily distinguished. Figures 7(*a*) and 7(*b*) show the evolution of bubbles for $\delta = 0.3$ and 0.6, respectively. As $\delta = 0.3$, after the liquid jet penetrates the lower bubble wall ($t = 1.701$), an obvious protrusion is formed on the lower bubble surface, which indicates that the downward momentum of the liquid jet is significantly higher than the upward momentum of the lower bubble wall. As $\delta = 0.6$, the lower bubble surface is obviously concave upward driven by buoyancy in the collapse stage. At $t = 1.701$, two opposite liquid jets are observed, but the upward momentum of the bubble plays a dominant role. After the two jets collide, the upward liquid jet continues to develop upward, creating a protrusion on the upper bubble surface. Unlike the case in figure 6, the bubble has significant downward or upward momentum at the collapse stage under these two δ. Next, we compare the pressure distribution and velocity field surrounding the bubble at the moment of jet impact under the three δ, as shown in figure 7(*c*). As δ increases, the high-pressure zone around the bubble gradually transitions from top-to-bottom. When δ is 0.461, this high-pressure area surrounds the right bubble surface, which confirms that the bubble is closest to the 'vertically neutral collapse' state under this δ.

If we use the δ calculated directly by the 'Blake criterion', the buoyancy effect of the bubble is relatively weak ($\delta = 0.442$). Figure 8 shows the bubble shapes at the moment of

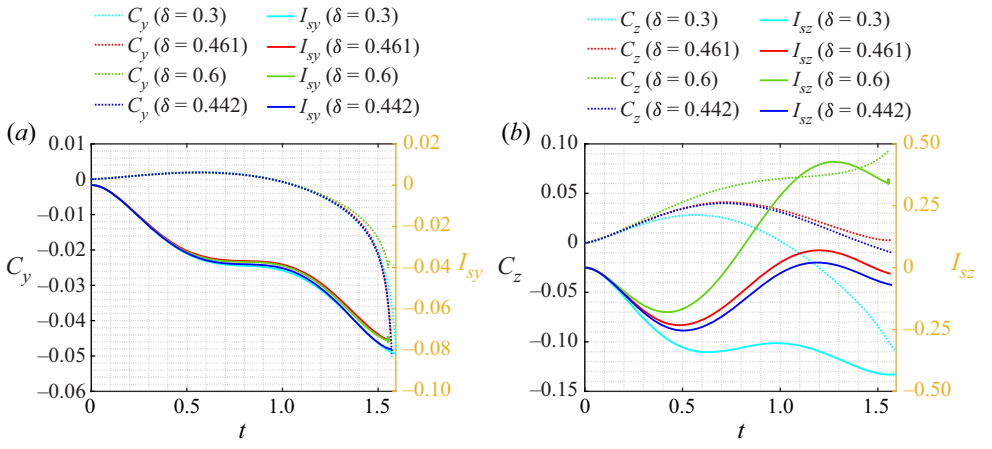

Figure 8. Time history curves of the bubble centre and Kelvin impulse in numerical simulations for different buoyancy parameters.

the jet impact, the time-history curves of the centroid and the Kelvin impulse of the bubble under four δ. The horizontal displacement of the bubble C_y is very small during most of the pulsation period due to the downward liquid jet, except when the bubble migrates towards the wall significantly at the end of the collapse. The horizontal Kelvin impulse of the bubble I_{sy} always remains negative, which is the reason why the bubble decelerates away from the wall in the first half of the cycle and accelerates towards the wall in the last half. The vertical migration of the bubble gradually changes from downward to upward with the increase in δ. In the early stage of bubble expansion, I_{sz} is negative, but I_{sz} gradually becomes positive at the late stage of bubble collapse for $\delta = 0.6$ and 0.461, resulting in the deflection in the direction of the vertical bubble migration. When the bubble reaches the vertically neutral collapse, I_{sz} at the end of the bubble collapse is close to zero ($|I_{sz}| < 0.03$). Here, I_{sz} at the end of the bubble collapse (0.024) is closer to zero for $\delta = 0.461$ than for the other three δ values. These results confirm that using our derived δ can predict the vertically neutral collapse of the bubble more accurately in this γ_f and γ_w. As the bubble gradually approaches the vertically neutral collapse, C_z and I_{sz} decrease relative to C_y and I_{sy}, respectively.

Next, we discuss the morphological changes of the bubble when γ_f and γ_w decrease. Figure 9 shows the bubble shapes at the collapse stage when the bubble is closer to the wall ($\gamma_f = 1$, $\gamma_w = 1.5$ and 0.9). When $\gamma_w = 1.5$, compared with figure 6, the right bubble surface shrinks faster relative to the left part, resulting in the position of jet impact being closer to the right extremity of the bubble, as shown in figure 9(*a*). When γ_w is less than 1 ($\gamma_w = 0.9$, as shown in figure 9*b*), the bubble surface close to the wall is flattened and the right lower surface of the bubble is also concave upward at the end of the bubble collapse, but the curvature of the upward concave surface is very small compared with the inclined downward liquid jet. Thus, we still regard this bubble collapse as the 'formally downward jet'. At the moment of jet impact ($t = 1.614$), the curvature of the right surface of the bubble becomes high due to the local opposite developing direction of the bubble walls; thus, a focused local high-pressure zone is generated on the right extremity of the bubble. Had the simulations been allowed to continue, the right extremity of the bubble would splash and develop towards the wall.

Figure 10 shows the jetting behaviour of the bubble nearer to the free surface for $\gamma_f = 0.8$ and $\gamma_w = 1.8$, 1.3 and 0.8. When $\gamma_w = 1.8$, the bubble produces a downward

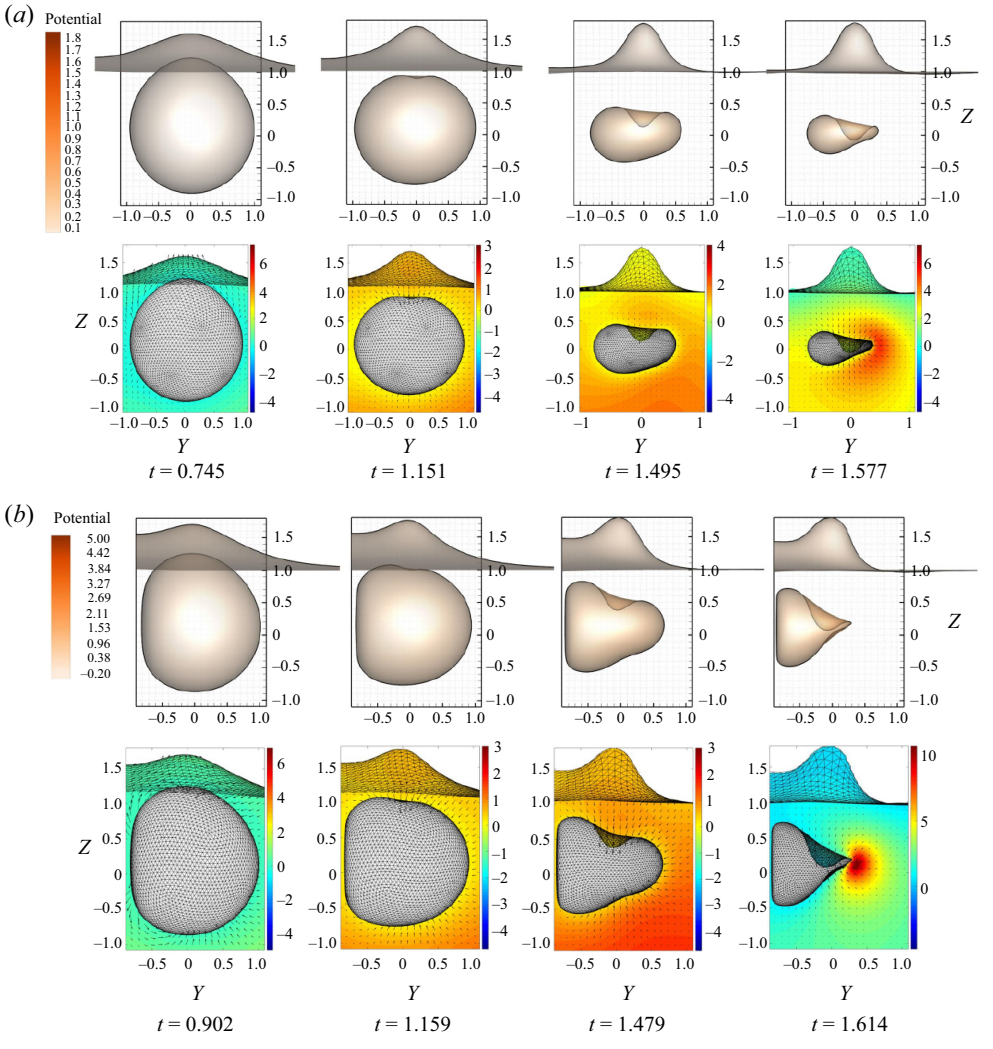

Figure 9. Bubble shape and surrounding pressure distribution at typical moments for (*a*) $\gamma_f = 1$, $\gamma_w = 1.5$ and $\delta = 0.472$ and (*b*) $\gamma_f = 1$, $\gamma_w = 0.9$ and $\delta = 0.515$.

jet under the action of the local high-pressure zone between the bubble and the free surface. Simultaneously, the higher hydrostatic pressure below the bubble also drives the lower bubble surface to collapse at a high speed. The pressure distribution surrounding the bubble is similar to the situation in figure 6, but the bubble shape is more symmetrical in the horizontal direction due to stronger free surface effects. As γ_w decreases ($\gamma_w = 1.3$), the bubble assumes a more asymmetric shape at the collapse stage, and the jet is more inclined to the wall under the action of the more asymmetric pressure and velocity field. When γ_w is less than 1 ($\gamma_w = 0.8$), the bubble surface close to the wall is flattened and the downward liquid jet is more inclined to the wall. At the moment of jet impact, a focused local high-pressure zone is formed on the side of the bubble farther away from the wall, which is similar to figure 9(*b*). However, for this γ_f, the stronger free surface effect causes the liquid jet to develop downward more fully. It could be learned from the values of δ provided in figures 9 and 10 that (4.8) overestimates the buoyancy effect required for the vertically neutral collapse of the bubble in the near boundary region.

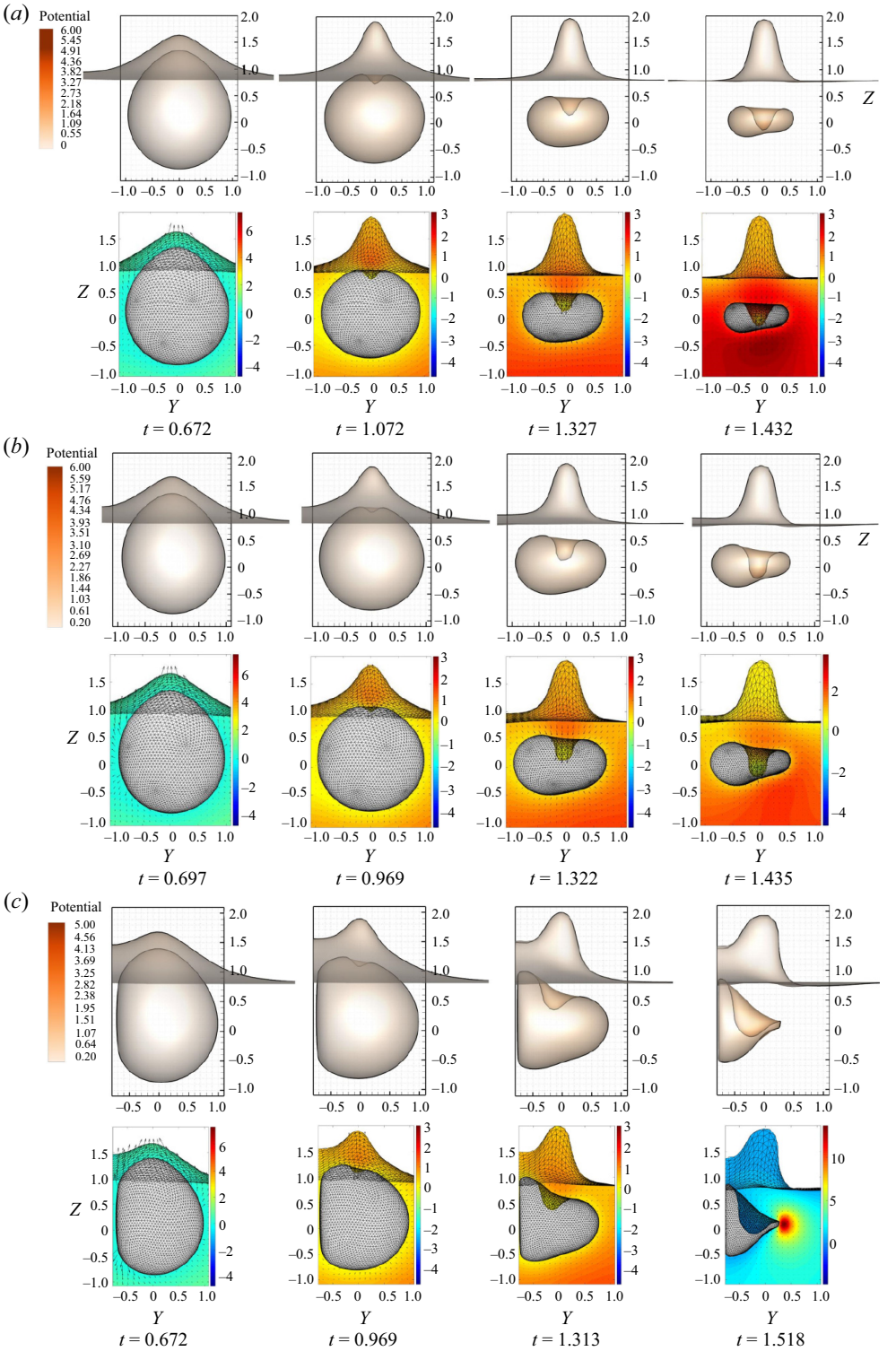

Figure 10. Bubble shape and surrounding pressure distribution at typical moments for (*a*) $\gamma_f = 0.8$, $\gamma_w = 1.8$ and $\delta = 0.560$; (*b*) $\gamma_f = 0.8$, $\gamma_w = 1.3$ and $\delta = 0.562$; and (*c*) $\gamma_f = 0.8$, $\gamma_w = 0.8$ and $\delta = 0.565$.

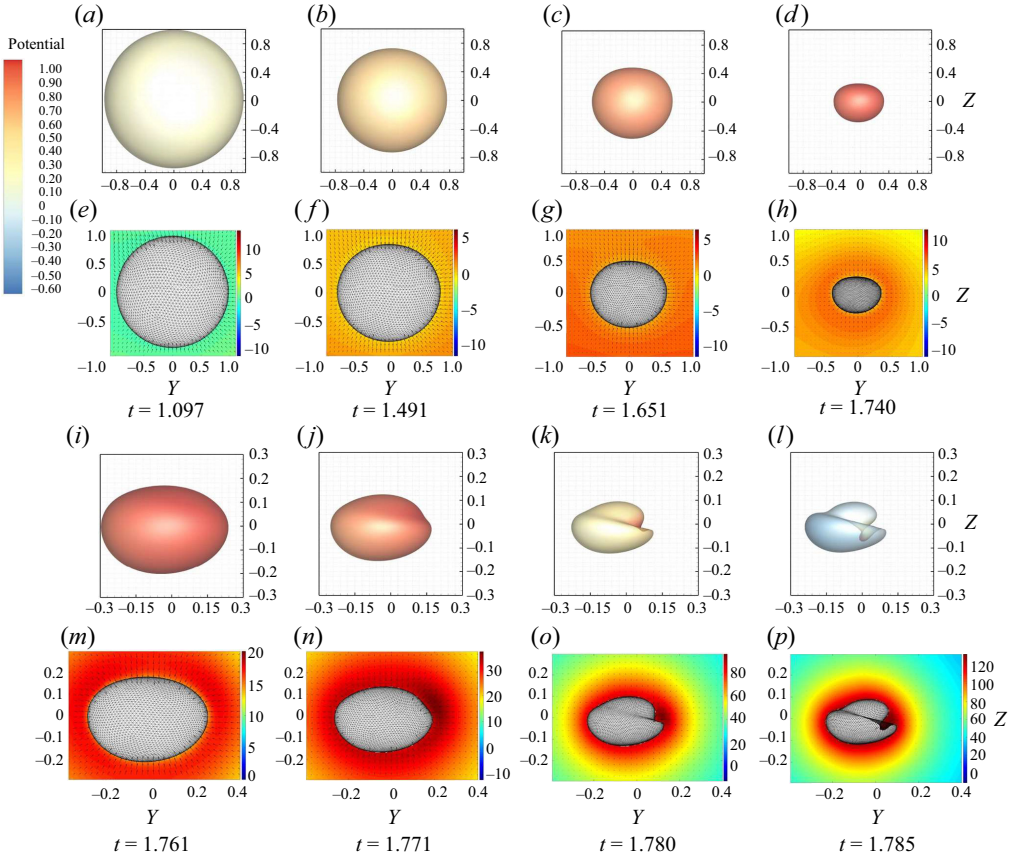

Figure 11. Bubble behaviour and surrounding pressure distribution at the collapse stage for $\gamma_f = 2$, $\gamma_w = 4$ and $\delta = 0.231$.

7.2. *Annular collapse*

Figure 11 shows the bubble behaviour and surrounding pressure distribution at the collapse stage when $\gamma_f = 2$, $\gamma_w = 4$ and $\delta = 0.231$ (the lift of the free surface is very weak; thus, it is not shown, and the same is true in the following pictures). In this case, the effect of the free surface in the vertical direction decreases, so the corresponding buoyancy is also weaker compared with that in figure 6. The liquids above and below the bubble flow more quickly than on the left and right sides during the bubble collapse. Thus, the bubble takes the shape of a horizontally placed egg (Frames 4–5). As a result, the greater curvature of the bubble surface near and away from the wall subsequently causes a faster contract velocity, which is the same result as Lauterborn's statements (Lauterborn 1982) on the pulsating velocity of the bubble: the bubble surface with higher curvature shrinks quicker and is more prone to jets. An asymmetric annular jet (Frame 7) is formed under the action of two local high-pressure zones on the left and right sides (Frames 5 and 6), in which the right high-pressure zone is stronger because the effect of the sidewall causes the bubble surface farther from the wall to contract faster. At $t = 1.785$ (Frame 8), the annular jet far from the sidewall is concave inward accompanied by an oblique downward liquid jet. In this pattern, an annular jet forms during bubble collapse. This produces a bulge with a high curvature above the bubble, which we call 'annular collapse'.

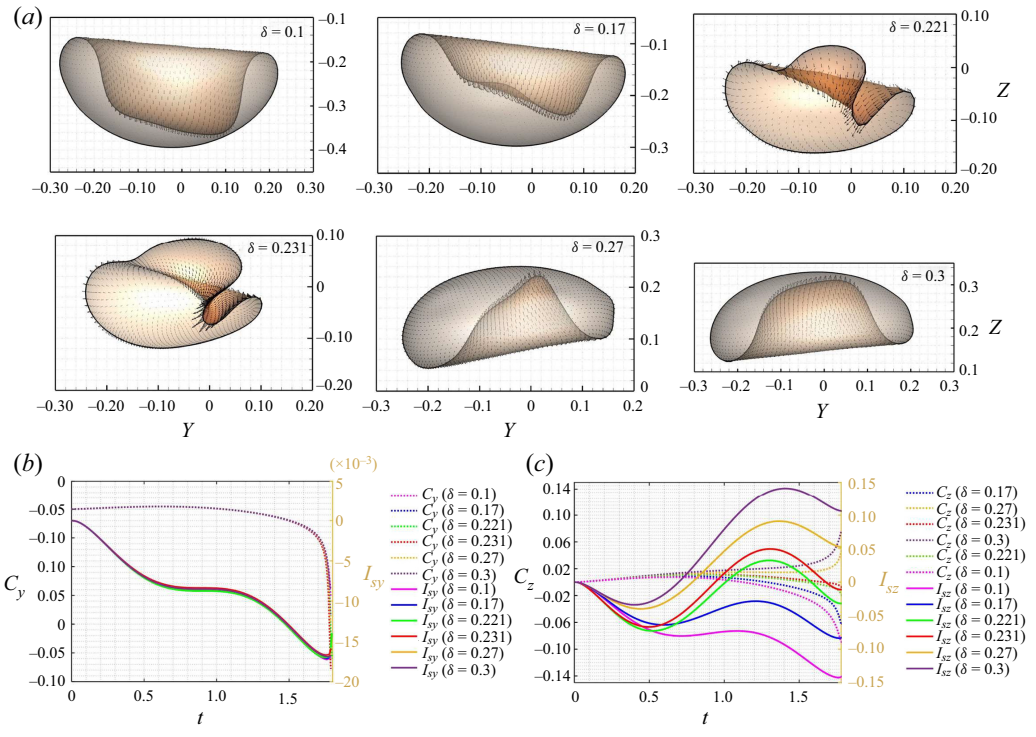

Figure 12. Comparison of bubble shapes for increasing buoyancy parameters when $\gamma_f = 2$ and $\gamma_w = 4$: (*a*) bubble shapes; (*b*) time history curves of the bubble centre; (*c*) time history curves of the Kelvin impulse of the bubble.

The bubble morphology, the time-history curves of the geometric centre and the Kelvin impulse are provided for increasing δ in figure 12. As shown in figure 12(*a*), for the case of small buoyancy, the bubble produces a wide downward jet ($\delta = 0.1$); as the buoyancy increases, the tip of the downward liquid jet begins to bulge upward ($\delta = 0.17$), and this bulge gradually becomes apparent as the buoyancy continues to increase until the bubble produces an annular jet ($\delta = 0.221$ and 0.231). Furthermore, the increasing δ causes the liquid jet to develop upward entirely ($\delta = 0.27$ and 0.3). Moreover, the greater δ leads to a wider upward jet. The horizontal displacement and Kelvin impulse of the bubble are relatively small under these buoyancy parameters. Here, $\delta = 0.221$ is obtained directly using Blake's criterion, and $\delta = 0.231$ is calculated by (4.8), under which C_z and I_{sz} at the end of the bubble collapse are closer to zero than for the other δ values.

Figure 13 illustrates two examples of the bubble profiles and the surrounding pressure distribution when the bubble moves away from the sidewall ($\gamma_f = 2$, $\gamma_w = 6$, 8). In the first case, as shown in figure 13(*a*), the right side of the bubble collapses quicker than the left, but the asymmetry of the annular jet decreases distinctly relative to that in figure 11. The decrease in the influence of the sidewall leads to gradual weakening in the oblique downward development of the annular jet. In the second case, as shown in figure 13(*b*), the bubble assumes an almost symmetrical 'gourd' shape with the symmetrical pressure distribution surrounding the bubble, and similar results in axisymmetric numerical simulation near a single free surface are also modelled and discussed in the work of Wang *et al.* (1996*a*).

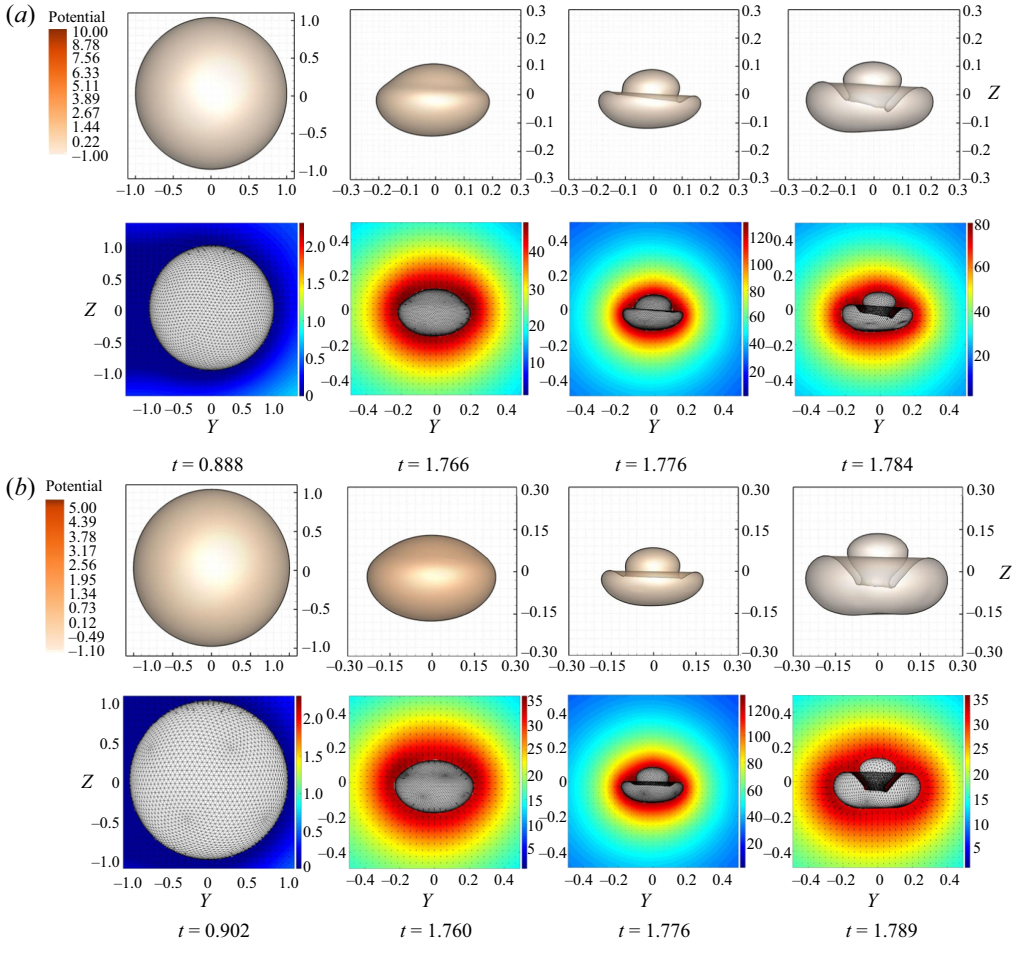

Figure 13. Bubble shape and surrounding pressure distribution at typical moments for (*a*) $\gamma_f = 2$, $\gamma_w = 6$ and $\delta = 0.224$ and (*b*) $\gamma_f = 2$, $\gamma_w = 8$ and $\delta = 0.223$.

We then compare the collapse behaviour of the bubble in the 'annular collapse' pattern for different γ_f ($\gamma_w = 5$, $\gamma_f = 1.5$, 1.75, 2, 2.25) in figure 14. The velocity vector and pressure distribution surrounding the bubble in the first case are given here, and others can be found in Appendix B. The four frames for each case correspond to the maximum bubble volume, jet formation, jet development and jet impact. A smaller γ_f indicates that the two opposing 'forces' acting on the bubble in the vertical direction are stronger, causing the bubble to be compressed flatter during jet development. The annular jet is generated later with the increase in γ_f because the 'forces' acting on the bubble surface are smaller. As shown in figure 14(*a*), the annular jet is generated under the action of the left and right local high-pressure zones above the bubble. The formation position of the annular jet gradually moves downward along the bubble surface with increasing γ_f, as illustrated in figures 14(*b*)–14(*d*). During jet development, the bulge generated above the annular jet becomes more pronounced with the increase in γ_f. When $\gamma_f = 2.25$, the bubble rebounds in volume at jet impact. Thus, the jet cannot contact the lower bubble surface, as seen in figure 14(*d*); the annular jet farther away from the wall is inclined downward, and the bubble profile becomes asymmetrically driven by the more asymmetric pressure field

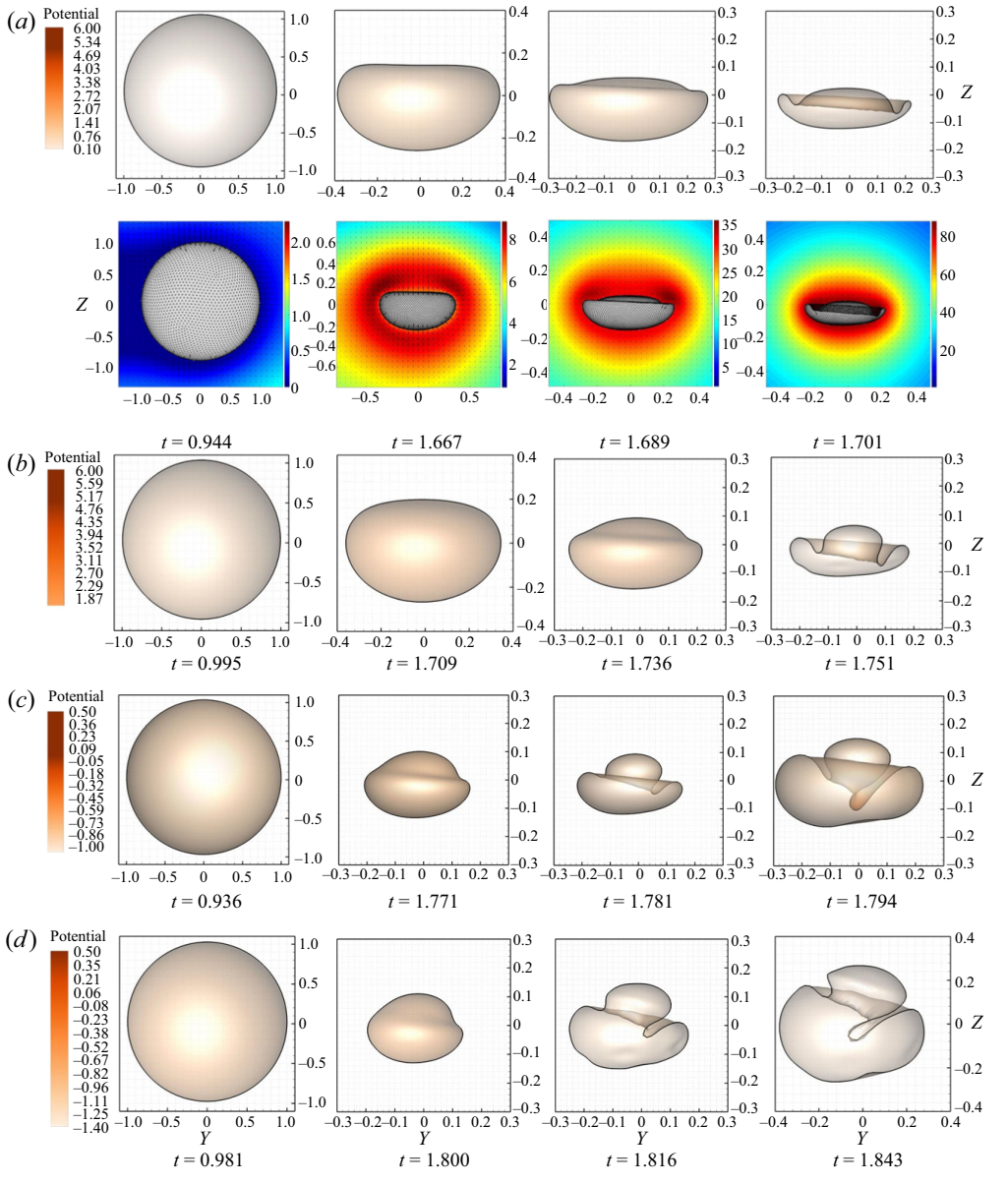

Figure 14. Comparison of the bubble shapes at typical moments for (*a*) $\gamma_f = 1.5$, $\gamma_w = 5$ and $\delta = 0.298$; (*b*) $\gamma_f = 1.75$, $\gamma_w = 5$ and $\delta = 0.257$; (*c*) $\gamma_f = 2$, $\gamma_w = 5$ and $\delta = 0.227$; and (*d*) $\gamma_f = 2.25$, $\gamma_w = 5$ and $\delta = 0.203$.

compared with the other cases (see Appendix B). Thus, we conclude that a smaller γ_f and a larger γ_w cause a more symmetrical annular jet.

7.3. *Horizontal jet*

Since the bubble moves farther away from the free surface, the buoyancy effect required for vertically neutral collapse decreases. Figure 15 shows the collapse process of the bubble generated far from the free surface and close to the sidewall for $\gamma_f = 4$, $\gamma_w = 2$

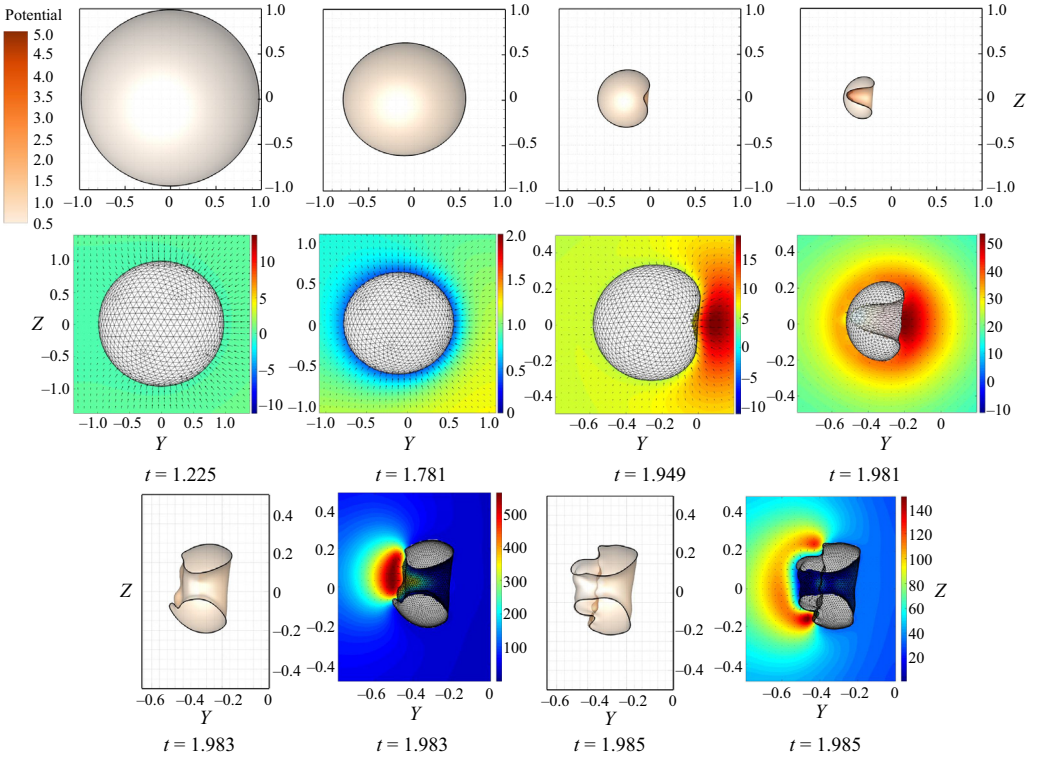

Figure 15. Collapse behaviour of the bubble at the collapse stage for $\gamma_f = 4$, $\gamma_w = 2$ and $\delta = 0.145$.

and $\delta = 0.145$. Due to the relatively weak effect of the free surface and buoyancy, the bubble maintains a spherical contraction at the early stage of bubble collapse. At $t = 1.949$ (Frame 3), the bubble surface farther away from the sidewall sags inward under the action of the local high-pressure zone on the right, producing a liquid jet directed to the wall. The bubble is almost symmetrical about the horizontal plane, similar to those cases near a single rigid wall (Li *et al.* 2016). After the liquid jet penetrates the opposite bubble wall, it develops towards the wall, forming a protrusion on the bubble surface near the wall. At $t = 1.985$, the bubble appears as a 'butterfly' shape, and the protrusion increases in volume as the liquid jet develops towards the sidewall, causing the right part of the bubble to shrink away from the sidewall under the action of two local high-pressure zones at the root of the protrusion. We refer to the situation in which the liquid jet is directed towards the sidewall as the 'horizontal jet' pattern.

Figure 16 shows the bubble shape at the moment of jet impact, the time-history curves of the centroid position and the Kelvin impulse of the bubble for four different δ values, in which $\delta = 0.11$ is calculated by the 'Blake criterion' and $\delta = 0.145$ is obtained by (4.8). In figure 16(a), the liquid jet rotates clockwise with the increase in δ and is directed perpendicularly to the sidewall when $\delta = 0.145$. The centroid position and z-direction Kelvin impulse of the bubble at jet impact are closest to zero when $\delta = 0.145$, as illustrated in figure 16(b,c). The migration amplitude of the bubble towards the wall in this collapse pattern is significantly larger than that in the two previously mentioned patterns; I_{sy} at the end of the first cycle exceeds two times that in the previous two patterns. Therefore, in the 'horizontal jet' pattern, the bubble has the greatest potential to attack the wall.

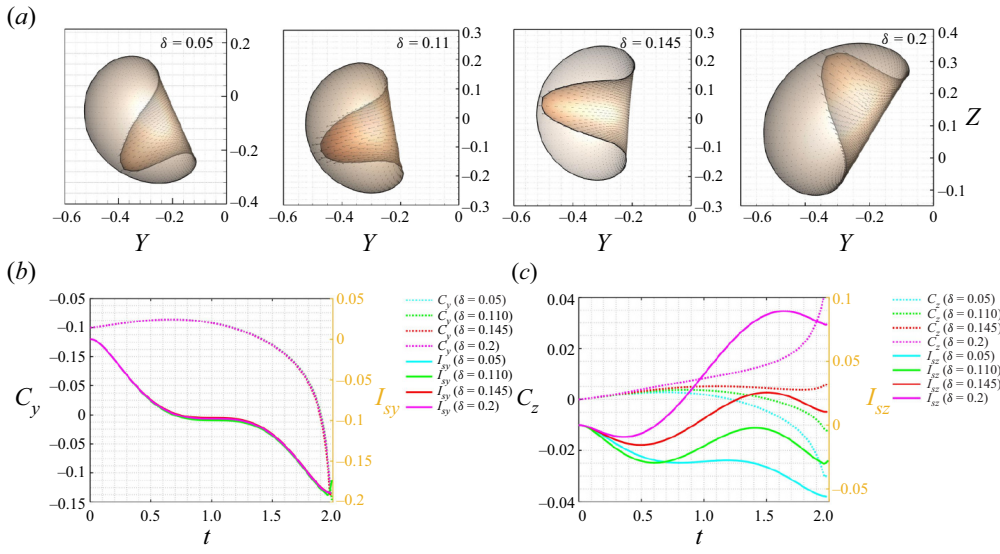

Figure 16. Comparison of bubble shapes for increasing buoyancy parameters when $\gamma_f = 4$ and $\gamma_w = 2$: (*a*) bubble shapes; (*b*) time history curves of the bubble centre; (*c*) time history curves of the Kelvin impulse of the bubble.

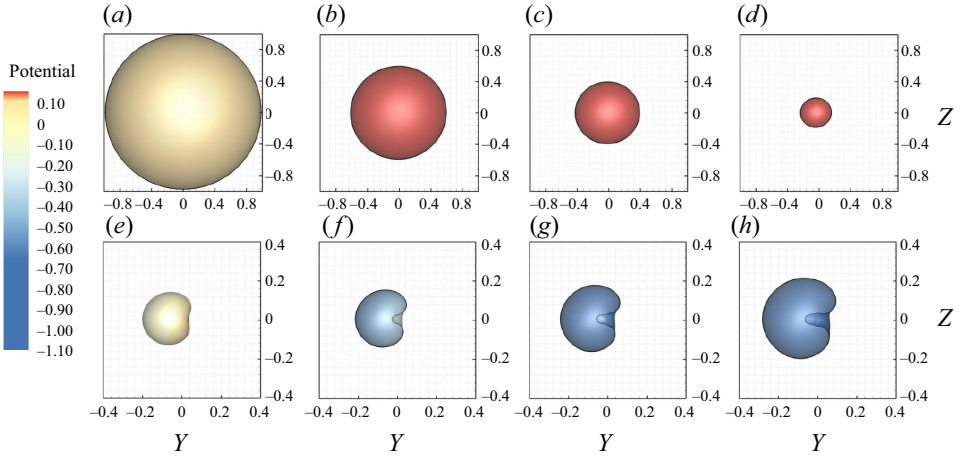

Figure 17. Collapse behaviour of the bubble at the collapse stage for $\gamma_f = 4$, $\gamma_w = 5$ and $\delta = 0.123$. The corresponding moments of the eight frames are 1.080, 1.725, 1.825, 1.881, 1.895, 1.899, 1.904 and 1.911, respectively.

7.4. *Weak jet*

In this section, the dynamics of the bubble far from the boundaries are discussed. Figure 17 shows the temporal development of the bubble for $\gamma_f = 4$, $\gamma_w = 5$ and $\delta = 0.123$. The bubble remains almost spherical throughout the contraction stage, which indicates that the effects of the boundaries and buoyancy are much weaker relative to the previous cases. The liquid jet is formed during the rebounding stage (Frame 5). Subsequently, due to the rapid expansion of the bubble, the development of the liquid jet towards the wall is hindered; thus, it is difficult for the liquid jet to penetrate the opposite bubble surface. In this case, the weak jet leads to the nearly spherical oscillation of the bubble. We compare the time history curve of the bubble radius with theoretical results in figure 18. The unified equation

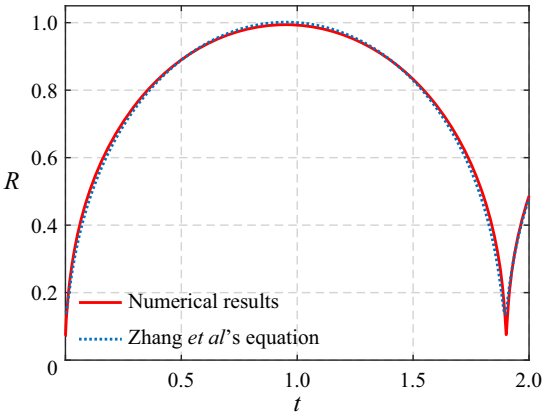

Figure 18. Comparison between the numerical and theoretical results of the bubble radius for $\gamma_f = 4$, $\gamma_w = 5$ and $\delta = 0.123$.

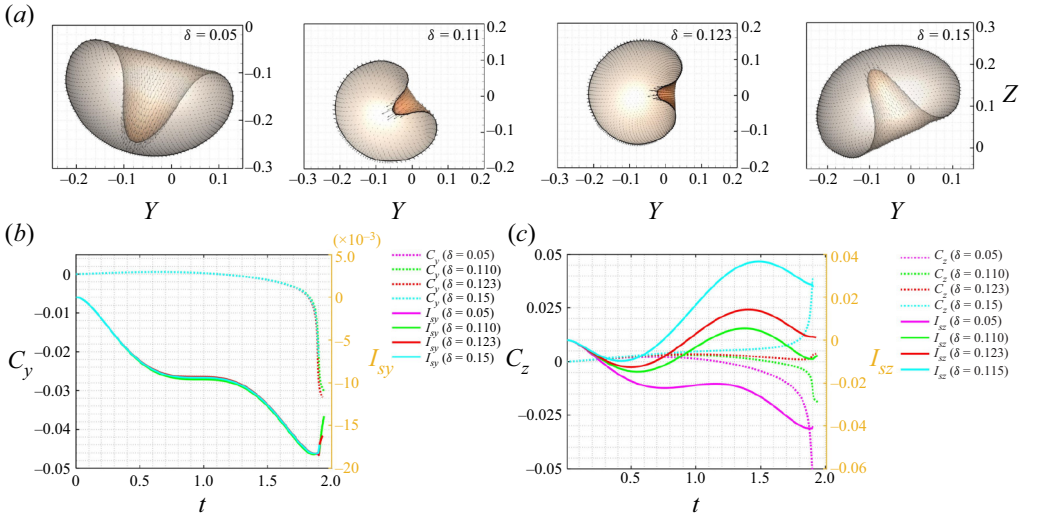

Figure 19. Comparison of bubble shapes for increasing buoyancy parameters when $\gamma_f = 4$ and $\gamma_w = 5$: (*a*) bubble shapes; (*b*) time history curves of the bubble centre; (*c*) time history curves of the Kelvin impulse of the bubble.

of the oscillation bubble proposed by Zhang *et al.* (2023*a*) is employed:

$$\left(\frac{C-\dot{R}}{R}+\frac{\mathrm{d}}{\mathrm{d}t}\right)\left[\frac{R^2}{C}\left(\frac{1}{2}\dot{R}^2+\frac{1}{4}v^2+H\right)\right]=2R\dot{R}^2+R^2\ddot{R}, \tag{7.1}$$

where C is sound speed in water; R, $\dot{R}$ and $\ddot{R}$ are bubble radius, oscillation velocity and acceleration, respectively; v denotes the migration velocity of the bubble; and H is the enthalpy difference at the bubble surface. To match our numerical results based in the incompressible fluid domain, the sound speed C needs to be infinity. In addition, H is modified to account for the influence of boundaries by adding three mirrored bubbles similar to that in figure 1.

The numerical bubble radius agree with the theoretical results well, which means that the evolution of the bubble in this pattern is similar to spherical bubble dynamics. We refer to the case in which the bubble resembles spherical oscillations as the 'weak jet' pattern.

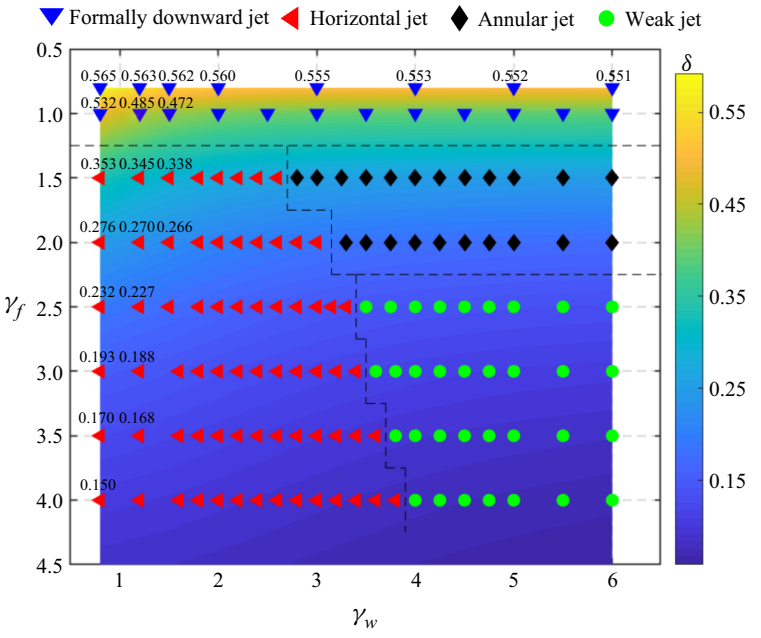

Figure 20. Classification of different collapse patterns for the vertically neutral collapse of the bubble near the free surface and a vertical wall as a function of γ_w and γ_f. Four types of bubble behaviour are summarized: formally downward jet, annular collapse, horizontal jet, and weak jet. The heatmap represents the change in δ corresponding to the vertically neutral collapse for different distance.

Figure 19 shows the bubble profiles at the end of the bubble collapse for different δ, along with the centroid position and Kelvin impulse of the bubble, in which $\delta = 0.111$ and 0.123 are calculated with (4.9) and (4.8), respectively. Similar to that in figure 16, C_z and I_{sz} are closest to zero using our derived δ. Notably, when the bubble significantly deviates from the 'vertically neutral collapse' state, the liquid jet develops fully in the first cycle because the bubble is subjected to a stronger pressure gradient in the vertical direction. However, the vertical pressure gradient acting on the bubble surface reaches equilibrium when the bubble is close to the vertically neutral collapse state, and the horizontal pressure gradient is also very weak, resulting in a weak jet.

8. Discussion

8.1. *Classification*

We classify the vertically neutral collapse behaviour of bubbles for different γ_f and γ_w in figure 20 through systematic simulations, and the distribution of δ corresponding to various γ_f and γ_w is provided in the form of a heatmap. In the region close to the free surface, the required δ for the bubble to reach the vertically neutral collapse is significantly higher than in other regions. As γ_f or γ_w increases, the corresponding δ gradually decreases. The cases with an error of more than 0.03, such as that in figure 4, are marked with the corresponding value of δ, and the rest of the cases are obtained directly using (4.8). The dynamic characteristics of the bubble under the four collapse patterns are discussed in detail in the previous section and are not repeated here. The occurrence of the 'horizontal jet', which occupies most of the parameter space when the bubble is relatively far from the free surface, is important. The bubble in the 'horizontal jet' pattern has a

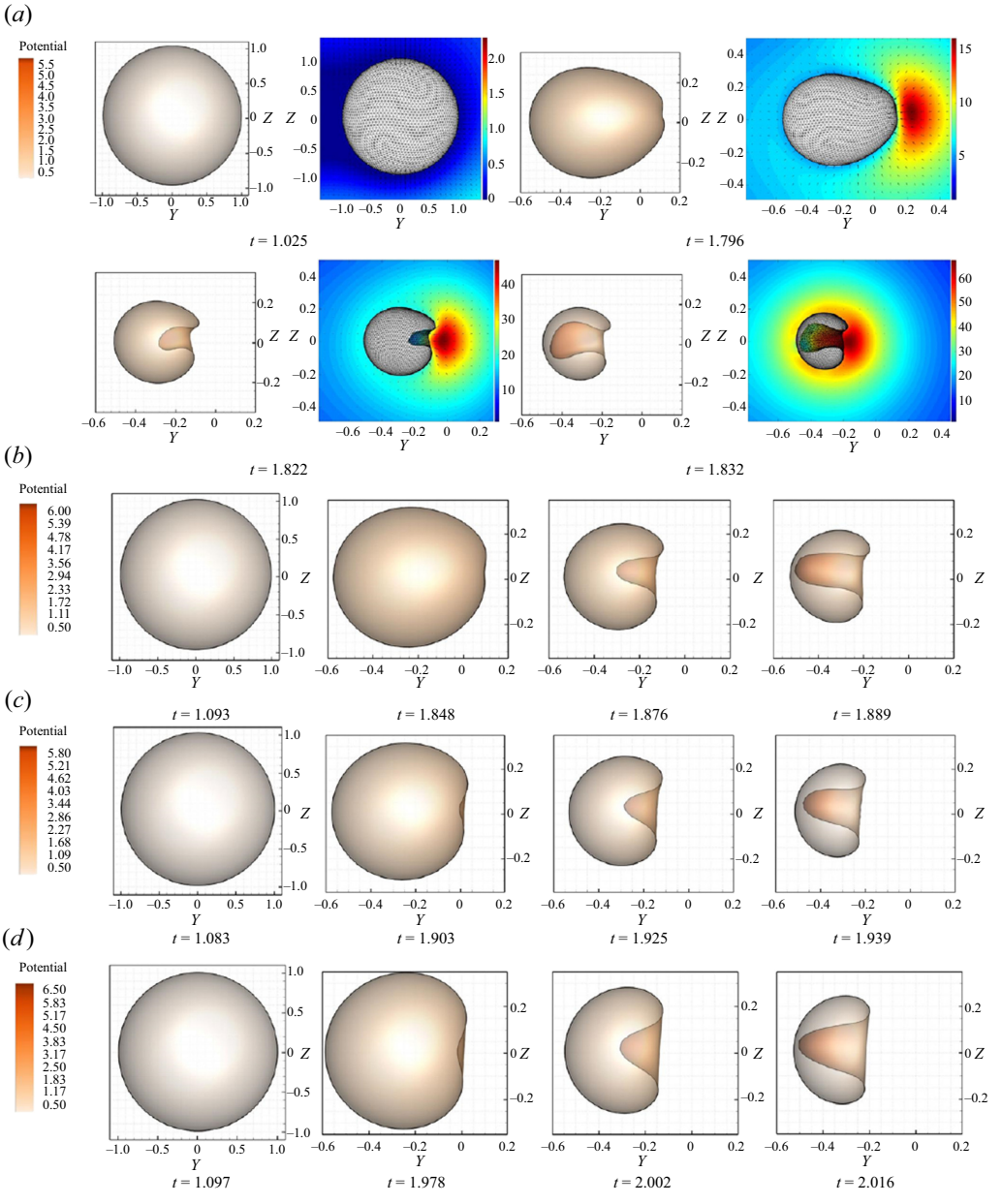

Figure 21. Comparison of the bubble shapes at typical moments for (*a*) $\gamma_f = 2$, $\gamma_w = 2$ and $\delta = 0.257$; (*b*) $\gamma_f = 2.5$, $\gamma_w = 2$ and $\delta = 0.215$; (*c*) $\gamma_f = 3$, $\gamma_w = 2$ and $\delta = 0.185$; and (*d*) $\gamma_f = 3.5$, $\gamma_w = 2$ and $\delta = 0.162$.

significant momentum towards the wall, as discussed in § 7.3. The dynamics characteristics of the bubbles at various γ_f when the 'horizontal jet' occurs are not entirely consistent, as seen from the transition between the collapse patterns. The 'annular collapse' or 'weak jet' transforms into the 'horizontal jet' at larger γ_w for larger γ_f. Therefore, a parametric analysis of the collapse characteristics of bubbles in the 'horizontal jet' pattern is carried out.

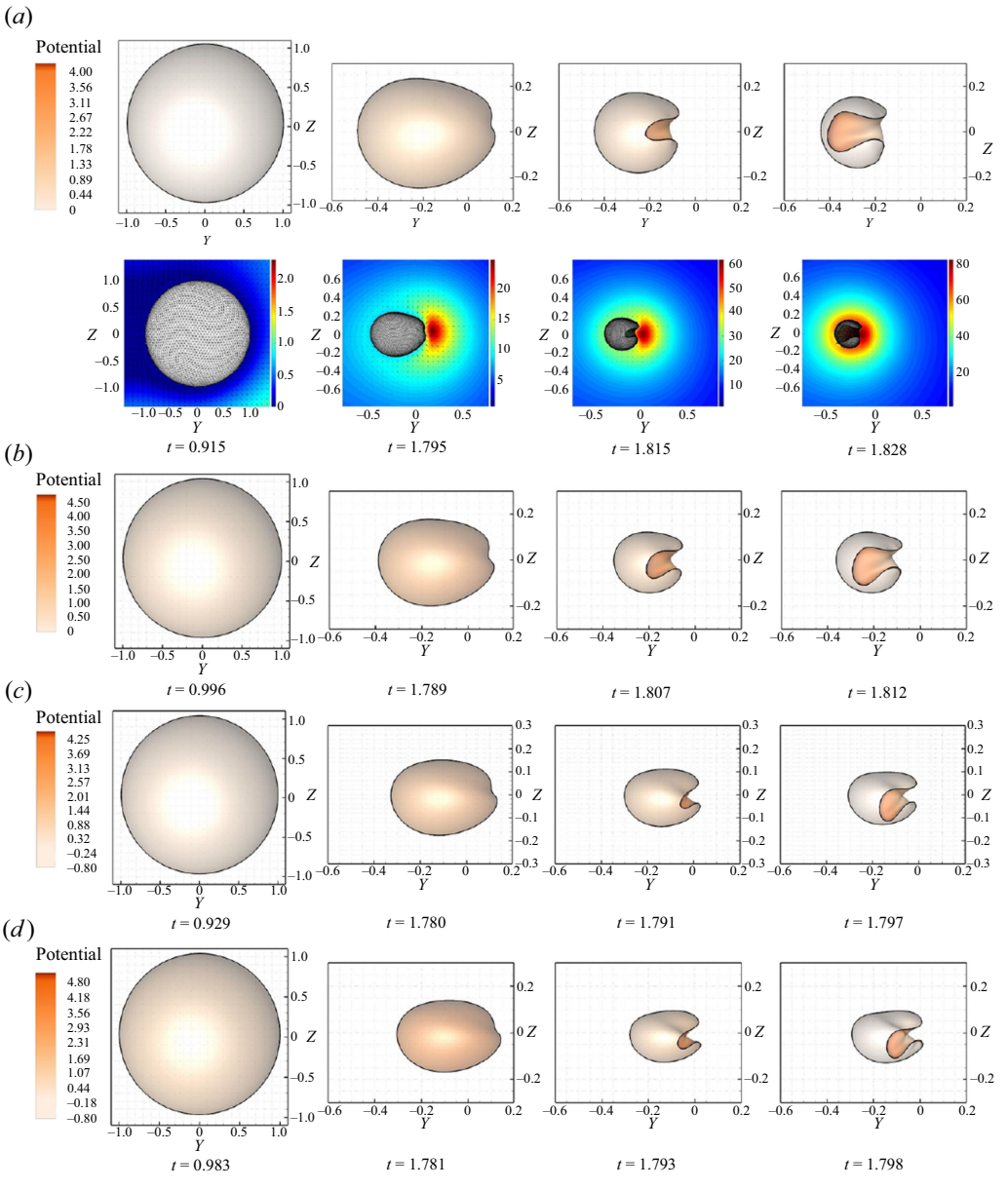

Figure 22. Comparison of the bubble shapes at typical moments for (*a*) $\gamma_f = 2$, $\gamma_w = 2.2$ and $\delta = 0.252$; (*b*) $\gamma_f = 2$, $\gamma_w = 2.6$ and $\delta = 0.245$; (*c*) $\gamma_f = 2$, $\gamma_w = 3$ and $\delta = 0.239$; and (*d*) $\gamma_f = 2$, $\gamma_w = 3.2$ and $\delta = 0.237$.

8.2. *Parametric analysis of the 'horizontal jet'*

8.2.1. *Bubble behaviour for different γ_w and γ_f*

Figure 21 compares the dynamic features of the horizontal jets for different γ_f at fixed γ_w ($\gamma_w = 2$, $\gamma_f = 2, 2.5, 3, 3.5$). The pressure distribution and velocity vector surrounding the bubble for $\gamma_f = 2$ are provided here, and others can be found in Appendix B. The liquid jets are all formed on the bubble surface farther away from the wall under the action of a fan-shaped local high-pressure zone. The smaller γ_f causes the bubble to be flatter at jet formations due to the stronger pressure gradient above and below the bubble, resulting in a

larger local curvature at the position of jet formation. During jet development, the contract velocity of the jet root cannot be maintained with the development of the jet tip towards the wall, causing the jet tip to be broad and the jet root to be thin at jet impact. With the increase in γ_f, the bubble surface at the position of jet formation gradually becomes flat with a thin jet tip and broad jet root, which is similar to the situation near a single rigid wall. Notably, regarding this γ_w, the jet impact occurs on the bubble surface nearer the sidewall.

We then illustrate the formation and development of the horizontal jets at different γ_w ($\gamma_f = 2$, $\gamma_w = 2.2$, 2.6, 3, 3.2) in figure 22. Additionally, we provide only the pressure distribution and velocity vector of the first case here. Compared with figure 21, the most prominent feature is that the horizontal jet no longer impacts the left bubble surface with the increase in γ_w but the lower bubble surface. We provide an explanation as follows: when the bubble is far away from the wall, the influence of the wall on the bubble is weaker than that of the free surface and buoyancy; thus, the longitudinal contraction of the bubble is more likely to affect the development of the horizontal jet. In figure 6, the vertically neutral collapse of the bubble is reached at the end of the bubble collapse, but the free surface makes the upper bubble surface more concave than the lower part. Similarly, for this γ_f, the bubble surface at the jet root is slightly concave downward in the case of $\gamma_w = 3$ and 3.2 under the action of the free surface, causing the local curvature of the bubble to be asymmetric to the horizontal plane. This is also reflected in the sloped local high-pressure zone at jet formation, as seen in figure 35 of Appendix B. The phenomenon of jets striking the lower bubble surface also indicates that the jet impact occurs earlier and that the bubble migration is hindered earlier.

8.2.2. *Moment of jet impact*

In the previous work of Supponen *et al.* (2016), the time interval from the jet impact to the minimum bubble volume Δt_{jet} is studied near a rigid wall for a Rayleigh bubble; however, in this study, the bubble with the high initial internal pressure does not continuously collapse as it gradually moves away from the wall; thus, the jet impact may occur earlier or later than the moment of the minimum bubble volume. Therefore, we choose to study the dimensionless moment of the jet impact. The dimensionless moment of the jet impact t_{jet} for different γ_f and γ_w is displayed in figure 23. Since the effect of the free surface is removed, the physical model degenerates to the classic situation near a single rigid wall, as shown by the yellow squares. The jet impact occurs earlier at a smaller γ_f because the free surface accelerates the pulsation of the bubble, which was demonstrated by the change in the kinetic energy of the volume of the liquid outside the bubble in the work of Gregorcic, Petkovsek & Mozina (2007). Here, t_{jet} increases with the decrease in γ_w since the rigid wall impedes the bubble pulsation, which has been observed in many works (Philipp & Lauterborn 1998; Vogel & Lauterborn 1988) on bubble–wall interactions. With increasing γ_f, the gap of t_{jet} for different γ_f gradually decreases, resulting from the decreasing forces acting on the bubble surface in the vertical direction. A slight increase in t_{jet} with γ_w occurs because the jet is generated late as γ_w is large; as a result, the bubble is in the rebounding stage during jet development, delaying the occurrence of the jet impact.

To further quantitatively explore the variation law of t_{jet} with the distance parameters, we define a relative moment of the jet impact t'_{jet}:

$$t'_{jet} = t_{jet} - t_f, \tag{8.1}$$

in which t_f is the bubble period for the case with the same γ_f and without the influence of the sidewall. Compared with t_{jet}, t'_{jet} can better reflect the effect of the rigid sidewall on

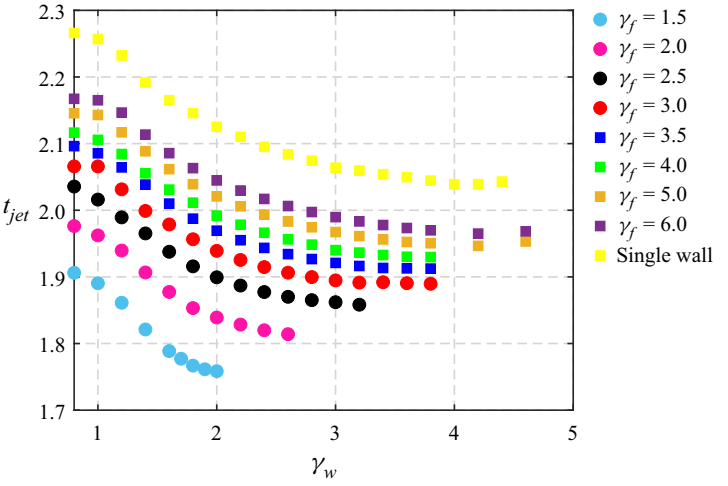

Figure 23. Dimensionless moment of the jet impacts for different γ_f and γ_w.

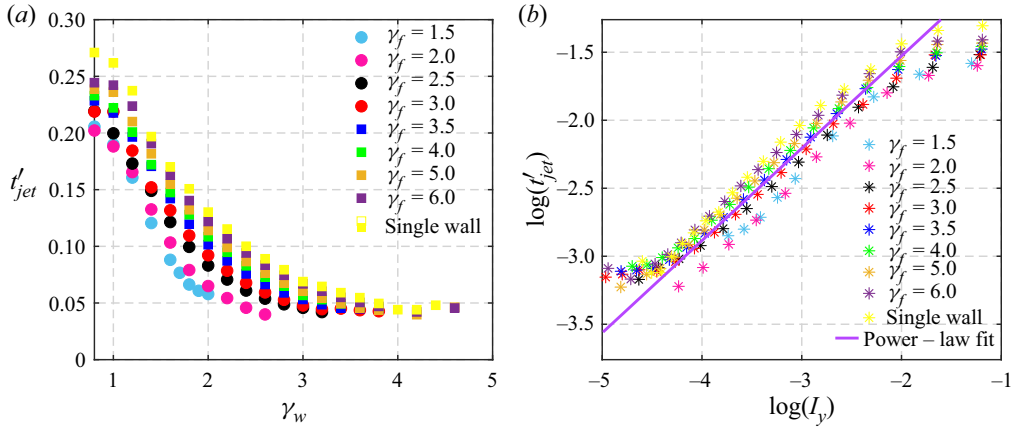

Figure 24. Variation in the relative moment of the jet impact t_{jet} as functions of (*a*) the bubble–wall distance γ_w and (*b*) theoretical Kelvin impulse in horizontal I_y in logarithmic form.

the bubble dynamics under different γ_f, and its value can be converted to a relatively small range with the change in γ_f.

Figure 24(*a*) shows the variation of t'_{jet} with respect to γ_w for different γ_f. The variation in t'_{jet} with γ_w almost converges to the cases near a single rigid wall when γ_f reaches 6. This means that the bubble–sidewall interaction is physically close to the classical case of a single rigid wall, although the free surface and weak buoyancy still combine to accelerate bubble collapse, as shown in figure 23. Furthermore, we present the variation in t'_{jet} with I_y in logarithmic form, as shown in figure 24(*b*). In most of the parameter space, $\log(t'_{jet})$ varies linearly with $\log(I_y)$, from which we can give the power law by fitting the data in figure 24(*b*):

$$t'_{jet} \propto I_y^{0.78}. \tag{8.2}$$

First, we conduct an idealized scaling analysis on the feature time. We take the feature length as the bubble radius R. According to the collapse velocity of the Rayleigh bubble,

the feature velocity satisfies $v = R^{-3/2}$. Therefore, the momentum can be scaled as $mv \propto R^3 \cdot R^{-3/2} = R^{3/2}$. The Kelvin impulse of the bubble is proportional to the momentum, $mv \propto I_y$, so the feature time t and Kelvin impulse satisfy the power law: $t \propto I_y^{5/3}$. Supponen *et al.* (2016) provided the power law of $\Delta t_{jet} \propto I_y^{5/3}$ by fitting Δt_{jet} of a Rayleigh bubble and some experimental data, which is consistent with the result of scaling analysis. The Δt_{jet} decays significantly faster with γ_w than with t'_{jet} because the moment of the jet impact gradually approaches the minimum bubble volume as γ_w increases. However, in this study, the time gap between the jet impact and t_f always exists, resulting in a significantly smaller exponential coefficient. In addition, it is worth noting that t'_{jet} deviates significantly from the power law as $\log(I_y) < -4.5$ or $\log(I_y) > -2$. When $\log(I_y) < -4.5$, the bubble is far from the sidewall, so the bubble rebounds before the jet impact, as mentioned before, which delays the occurrence of the jet impact. When $\log(I_y) > -2$, the bubble is very close to the sidewall and begins to deviate from the spherical shape during the expansion phase. This causes the liquid jet to generate relatively earlier, which accelerates the occurrence of the jet impact.

8.2.3. *Jet velocity*

In this section, we discuss the variation law of the jet velocity v_{jet} (the velocity of the jet tip at jet impact) for different γ_f and γ_w, as shown in figure 25. As γ_f reaches 3, the changing trend is related to t_{jet}. Here, v_{jet} first increases and then decreases with increasing γ_w for fixed γ_f, except when the bubble is very close to the rigid wall ($\gamma_w < 1.5$), and v_{jet} fluctuates with the variation in γ_w. The fluctuation was also observed and confirmed near a single wall in the works of Tomita & Shima (1986) and Zhang *et al.* (2017). The γ_w corresponding to the peak jet velocity is consistent with the γ_{mw} corresponding to the minimum t_{jet} in figure 23; as explained in § 8.2.2, when the bubble rebounds in volume during jet development for large γ_w, the rapid expansion of the bubble delays the occurrence of the jet impact, resulting in the decreasing v_{jet} with increasing γ_w. When the bubble continuously contracts during the jet development for small γ_w, the liquid jet is accelerated constantly, causing v_{jet} to increase with increasing γ_w. Notably, the amplitude of the jet velocity when $\gamma_f < 3$ is higher than when γ_f reaches 3, which is attributed to the strong effect of the free surface and buoyancy on the jet development; the strong pressure acting on the bubble surface compresses the bubble to a smaller volume when the liquid jet is further accelerated, as illustrated in figures 21 and 22. As γ_f increases, the variation in the jet velocity with γ_w gradually approaches the situation near a single wall.

Furthermore, figure 25(*b*) shows the change law of $\log(v_{jet})$ with $\log(I_y)$. Similar to figure 24(*b*), $\log(v_{jet})$ changes linearly with $\log(I_y)$ over most of the parameter space, from which we can give the power law:

$$v_{jet} \propto I_y^{-0.44}. \tag{8.3}$$

Supponen's power law for the jet velocity of a Rayleigh bubble is $v_{jet} \propto I_y^{-1}$, which agrees with the result of scaling analysis but obviously overestimates the increasing rate of the jet velocity with γ_w because the Rayleigh bubble continuously accelerates to collapse even when γ_w exceeds 10; however, for bubbles with a high initial internal pressure in this study, the bubble rebounds in volume after collapsing to a larger size as γ_w exceeds approximately 3. Therefore, the exponential coefficient is significantly greater than -1. In addition, fluctuations in v_{jet} in the near-wall region cause v_{jet} to deviate significantly from the power law at $\log(I_y) > -2$. As $\log(I_y) < -4.5$, the liquid jet becomes relatively weak due to the large bubble–wall distance, and the bubble begins to expand before the

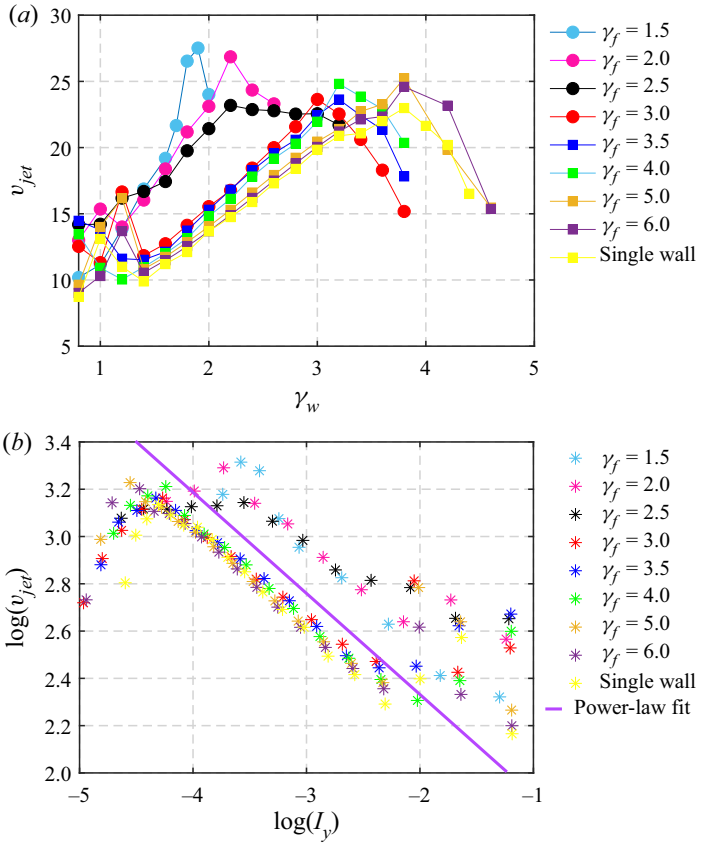

Figure 25. Variation in the jet velocity v_{jet} as functions of (*a*) the bubble–wall distance γ_w and (*b*) theoretical Kelvin impulse in horizontal I_y in logarithmic form.

jet impact, which corresponds to cases when γ_w exceeds 3 in figure 25(*a*). Thus, the jet impact is alleviated by the high pressure inside the bubble in the early stage of the second cycle, resulting in the jet velocity at the moment of jet impact decreasing with decreasing $\log(I_y)$.

8.2.4. *Bubble displacement*

Figure 26(*a*) displays the bubble displacement at jet impact D for different γ_f and γ_w, in which we ignore the bubble displacement in the vertical direction due to its weak effect (see Appendix C). The D increases slightly with increasing γ_f but shows a consistent downward trend with γ_w at all γ_f. To quantitatively describe the changing trend of D with respect to γ_w, we fit the data in figure 26(*a*) for all γ_f and obtain a power law:

$$D \propto \gamma_w^{-1.37}. \tag{8.4}$$

Furthermore, we show the variation in D with respect to I_y in logarithmic coordinates, as illustrated in figure 26(*b*). We can provide a power law with regards to D and I_y by fitting the data in figure 26(*b*):

$$D \propto I_y^{0.56}. \tag{8.5}$$

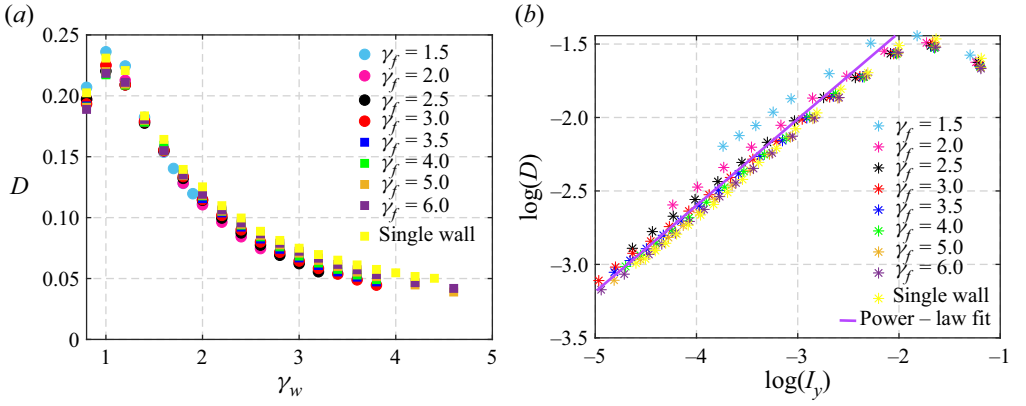

Figure 26. Variation in the bubble displacement at jet impact D as functions of (a) the bubble–wall distance γ_w and (b) theoretical Kelvin impulse in horizontal I_y in logarithmic form.

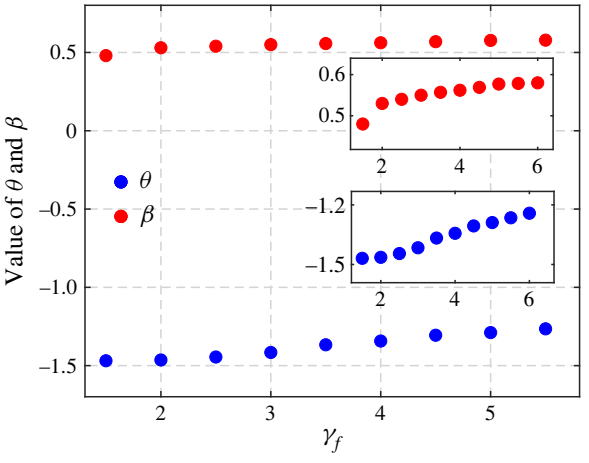

Figure 27. Variation of θ and β with respect to γ_f.

A notable feature of the bubble displacement is that the exponential coefficient of the above two power laws increases monotonically with increasing γ_f. Thus, we provide the two coefficients θ and β in figure 27 ($D \propto \gamma_w^{\theta} \propto I_y^{\beta}$). First, it is worth noting that Supponen *et al.* (2016) combined experiments and numerical simulations to provide a power law for the migration distance of a no-buoyancy bubble near a single rigid wall: $D \propto I_y^{0.6}$. As they stated, for real bubbles, the contraction speed at the minimum volume is smaller than that of the Rayleigh bubble, $v < R^{-3/2}$, so the power-law exponent is expected to be lower than the $2/3$ value obtained through scaling analysis. However, even so, β in our study does not reach 0.6, as figure 27 shows.

In fact, β is small when the bubble is close to the free surface, which indicates that the horizontal displacement of the bubble decays faster with γ_w than for larger γ_f. We learn from (4.6) that I_y is related only to γ_w if we ignore the effect of the free surface. Then, it is expected that $I_y \propto \gamma_w^{-2}$, resulting in $\theta = -2\beta$. However, as figure 27 shows, θ is much less than -2β, especially when γ_f is small. This is the consequence of the extra term in (4.6) caused by the free surface. The relation of $\theta < -2\beta$ illustrates that the free

surface reduces the momentum of the bubble migrating towards the wall. Even though the buoyancy balances out the effect of the free surface, the bubble is less likely to migrate towards the surrounding structures near the free surface. In addition, when γ_f is small, the collapse pattern gradually transitions from the 'horizontal jet' to the 'annular collapse' in which the horizontal displacement of the bubble in the first period is greatly weakened, as shown in figure 12. The position of the jet impact can also partly explain the variation trend of D. As figure 22 shows, the liquid jet impacts the lower surface of the bubble before it reaches the left wall of the bubble when $\gamma_f = 2$, delaying the continued increase in D.

It is expected that θ increases with increasing γ_f even if the bubble is far away from the free surface when 'annular collapse' does not occur. Since the smaller γ_f results in the bubble being subjected to greater 'forces' from above and below, the bubble is pressed in the vertical direction to a greater extent. As a result, the movement of the bubble in the horizontal direction is hindered and limited. As γ_f increases, β gradually approaches the 0.6 value obtained by Supponen for the case of no free surface and no buoyancy. In fact, when the influence of the free surface is removed, the bubble is no longer subjected to an additional pressure gradient in the direction parallel to the rigid wall. Thus, the bubble achieves vertically neutral collapse without the need for buoyancy. When the free surface is removed, as shown by the yellow marks in figure 27, β reaches 0.6 when θ is equal to -2β.

9. Summary and conclusion

In this paper, the vertically neutral collapse of a pulsating bubble (the buoyancy balances the effect of the free surface) near the free surface and a vertical rigid wall is systematically studied combined with theoretical and numerical methods. The BIM is adopted to simulate the bubble behaviour, and the free surface is treated as an open-domain area through a virtual vortex. Three key characteristic parameters are mainly studied: the bubble-free surface distance γ_f, bubble–wall distance γ_w and buoyancy parameter δ. Combined with the mirror point source/sink method, the Kelvin impulse of the bubble is derived to determine the relationship among the three parameters for vertically neutral collapse.

Kelvin impulse theory can accurately predict vertically neutral bubble collapse when the bubble is relatively far from the boundaries (see figure 4). As the value of δ for vertically neutral collapse at fixed γ_f and γ_w is determined, the collapse pattern of the bubble depends fully on γ_f and γ_w. Four collapse patterns are performed, namely, 'formally downward jet', 'annular collapse', 'horizontal jet' and 'weak jet'. The 'formally downward jet' originates from the strong interaction between the bubble and the free surface. Although the upper bubble surface is concave downward to produce a downward liquid jet, the lower surface has a considerable upward velocity at the end of the bubble collapse, resulting in the bubble oscillating without obvious momentum in the vertical direction during the rebounding phase. With the decrease in γ_w, the curvature of the bubble surface farther away from the wall becomes large at jet impact, resulting in a bubble with increasing momentum towards the wall. As $\gamma_w < 1$, the extremity of the bubble wall far away from the wall becomes very sharp at jet impact, and a focused local high-pressure zone is generated nearby. The 'annular collapse' indicates that an annular jet is generated at the end of the bubble collapse. The two local high-pressure zones generated during bubble collapse at the left and right extremities of the bubble cause the formation of a bulge with high curvature above the bubble. The smaller γ_f and the larger γ_w lead to a more symmetrical annular jet accompanied by a more symmetrical pressure distribution of the flow field. The 'weak

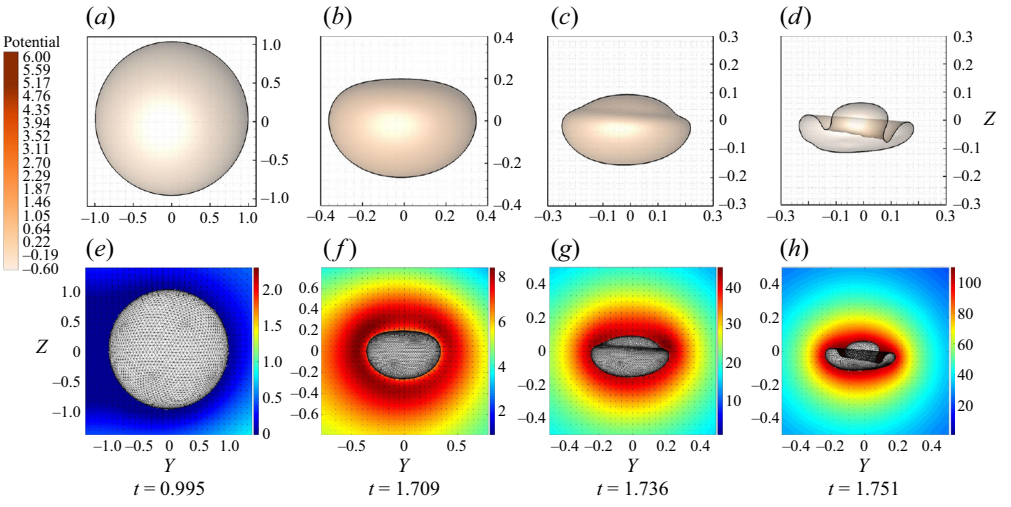

Figure 28. Bubble shape and surrounding pressure distribution at typical moments for $\gamma_f = 1.75$, $\gamma_w = 5$ and $\delta = 0.257$.

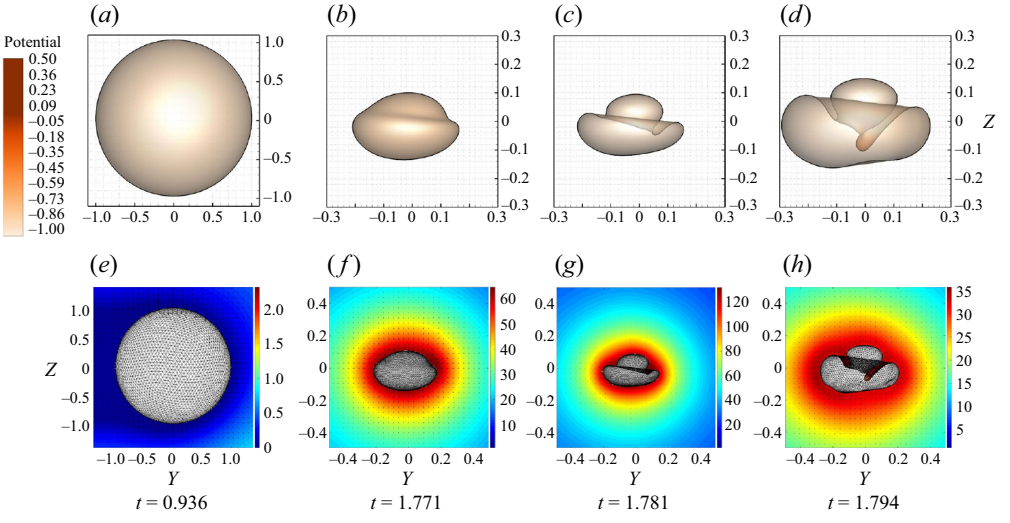

Figure 29. Bubble shape and surrounding pressure distribution at typical moments for $\gamma_f = 2$, $\gamma_w = 5$ and $\delta = 0.226$.

jet' occurs when the bubble is far from the boundaries and the liquid jet is developed late without penetrating the bubble surface.

Among the four collapse patterns, the 'horizontal jet' has the greatest potential to attack the wall. The Kelvin impulse and the bubble displacement towards the wall are much larger than the other three patterns at the late stage of bubble collapse. The moment of the jet impact t_{jet} increases with increasing γ_f and decreasing γ_w on the whole, but increases slightly with decreasing γ_w when the bubble is far from the free surface. This is the consequence of the bubble rebounding before the jet impact as γ_f is large, which also hinders the development of the liquid jet. As a result, the jet velocity v_{jet} increases first and then decreases with increasing γ_w, with γ_w corresponding to the peak velocity increasing

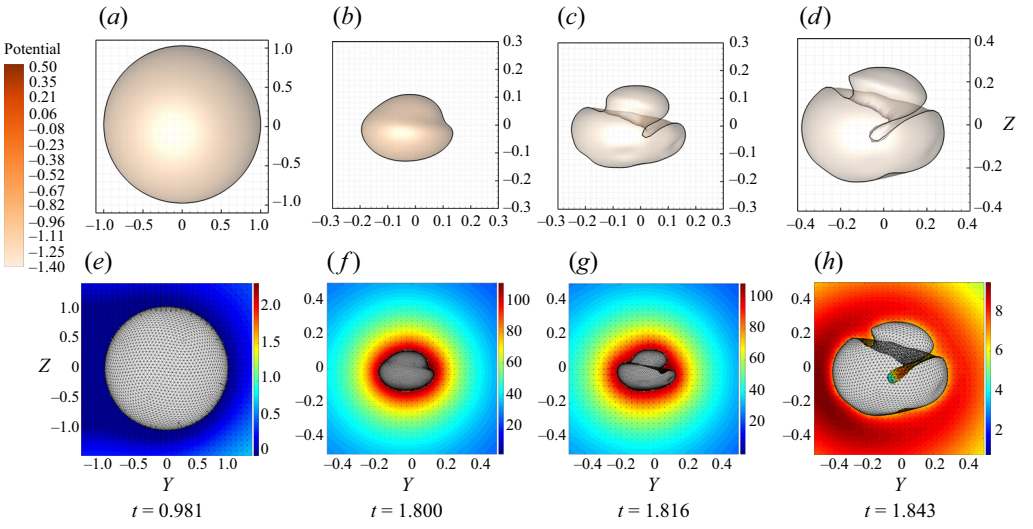

Figure 30. Bubble shape and surrounding pressure distribution at typical moments for $\gamma_f = 2.25$, $\gamma_w = 5$ and $\delta = 0.203$.

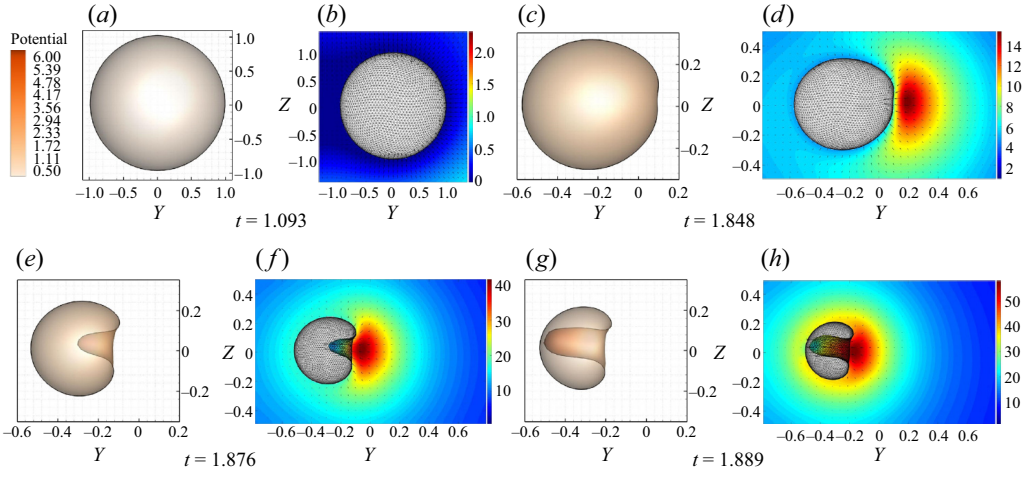

Figure 31. Bubble shape and surrounding pressure distribution at typical moments for $\gamma_f = 2.5$, $\gamma_w = 2$ and $\delta = 0.215$.

with increasing γ_f as γ_f is large. As γ_f is small, a peak of v_{jet} with increasing γ_w also exists due to the gradual transition of the collapse pattern.

In the 'horizontal jet' pattern, the power laws of the relative moment of the jet impact to the case of a single free surface t_{jet}, the jet velocity v_{jet} and the bubble displacement at jet impact D with respect to I_y are found when the bubble is relatively far from the rigid wall ($\log(I_y) < -2$): $t'_{jet} \propto I_y^{0.78}$, $v_{jet} \propto I_y^{-0.44}$, $D \propto I_y^{0.56}$. The high initial internal pressure of the bubble causes the power laws of t'_{jet} and v_{jet} to fail at a large γ_w ($\log(I_y) < -4.5$), and it is also an important reason why the power-law exponent of v_{jet} is significantly larger than the result of scaling analysis. The power-law exponent of the bubble displacement increases with increasing γ_f ($D \propto \gamma_w^{\theta} \propto I_y^{\beta}$) and converges to the case with a single wall.

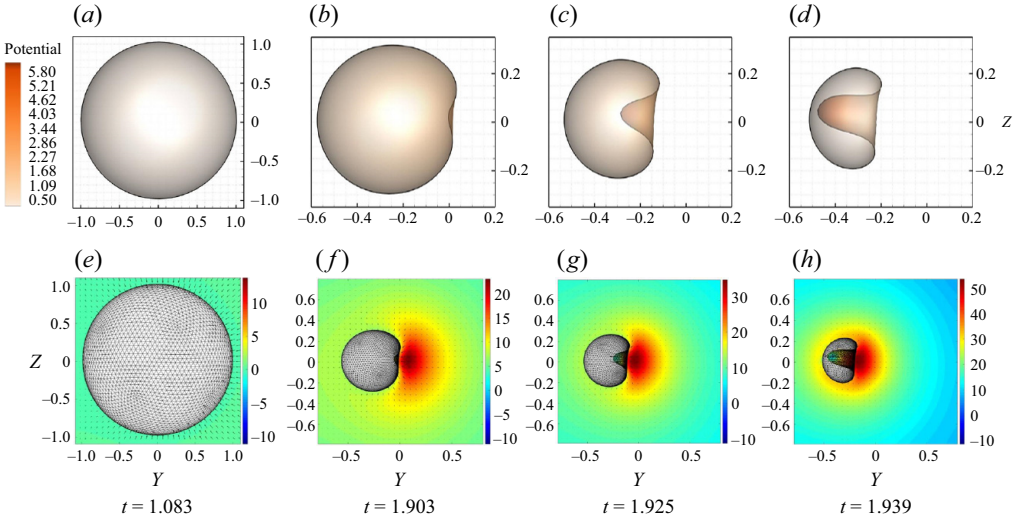

Figure 32. Bubble shape and surrounding pressure distribution at typical moments for $\gamma_f = 3$, $\gamma_w = 2$ and $\delta = 0.185$.

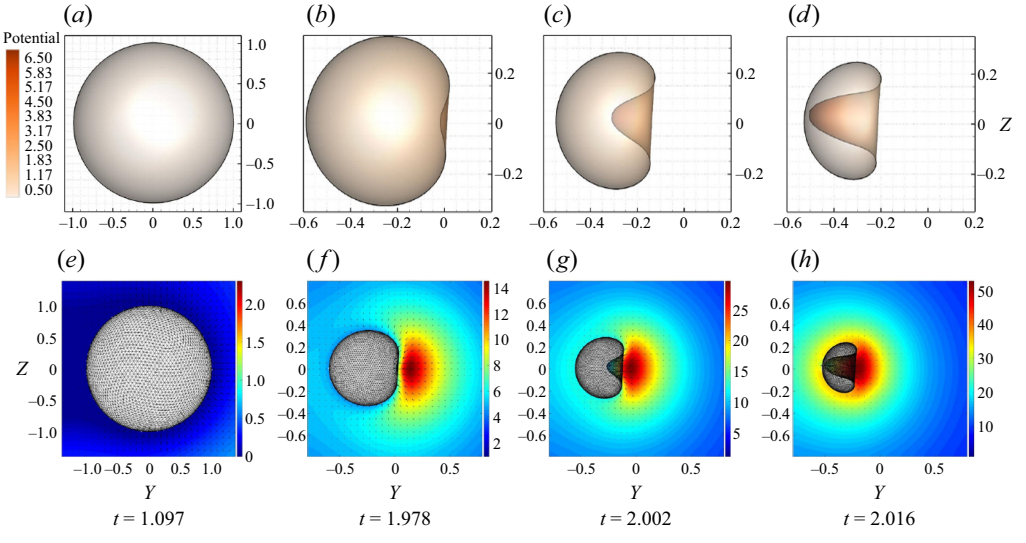

Figure 33. Bubble shape and surrounding pressure distribution at typical moments for $\gamma_f = 5$, $\gamma_w = 2$ and $\delta = 0.119$.

Scaling analysis indicates that the free surface reduces the momentum of the bubble migrating towards the sidewall, resulting in $\theta < -2\beta$. In addition, at small γ_f, the change in the jet behaviour, such as the position of the jet impact shifting from the left to lower bubble surface, is also responsible for the small θ.

Funding. This work is funded by the National Natural Science Foundation of China (nos. 52088102, 51979049) and the National Key R&D Program of China (no. 2022YFC2803500).

Declaration of interests. The authors report no conflict of interest.

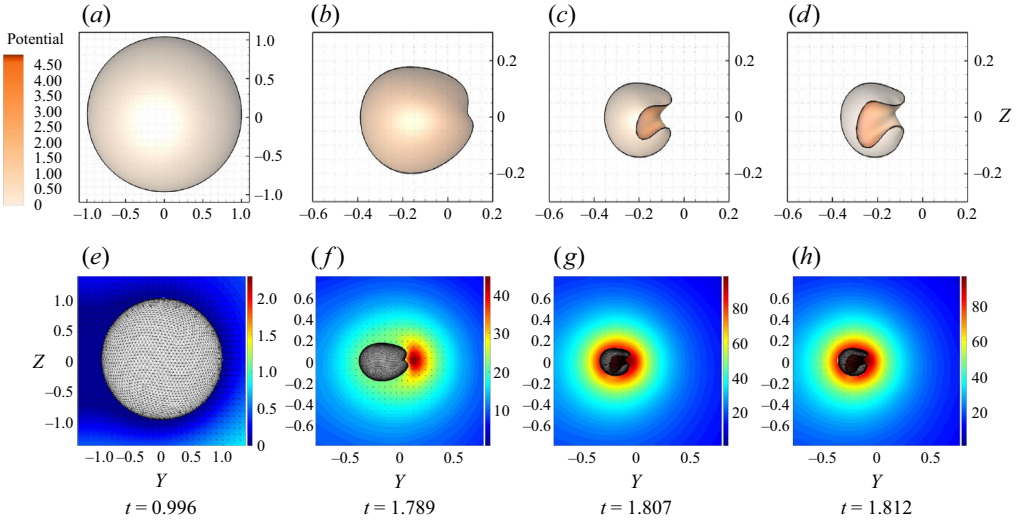

Figure 34. Bubble shape and surrounding pressure distribution at typical moments for $\gamma_f = 2$, $\gamma_w = 2.6$ and $\delta = 0.245$.

Author ORCIDs.
Shi-Min Li https://orcid.org/0000-0002-8290-7452;
A-Man Zhang https://orcid.org/0000-0003-1299-3049;
Pu Cui https://orcid.org/0000-0001-8179-1366;
Shuai Li https://orcid.org/0000-0002-3043-5617;
Yun-Long Liu https://orcid.org/0000-0001-9958-2757.

Appendix A. Supplement of the derivation of (4.8)

A polar coordinate system is established by taking the intersection point of the free surface and rigid wall in a two-dimensional plane as the origin, and the line between the point source/sink and the intersection point as the polar axis. Then, we have $\gamma^2 = \gamma_f^2 + \gamma_w^2$ and $\gamma_f = \gamma \sin(\omega)$. Thus, we let I_z be zero, and (4.7) can be transformed into

$$-\frac{2\sqrt{6}\pi}{9}\left[\left(\frac{1}{\gamma_f^2}+\frac{1}{(\gamma_f/\sin\omega)^2}\sin\omega\right)B\left(\frac{7}{6},\frac{3}{2}\right)-2\delta^2 B\left(\frac{11}{6},\frac{1}{2}\right)\right]=0. \tag{A1}$$

Simplifying the above equation, we obtain

$$\frac{1}{\gamma_f^2}\left(1+\sin^3\omega\right)B\left(\frac{7}{6},\frac{3}{2}\right)=2\delta^2 B\left(\frac{11}{6},\frac{1}{2}\right), \tag{A2}$$

based on which (4.8) can be obtained by converting the polar coordinate back to Cartesian coordinates.

Appendix B. Bubble shape and surrounding pressure distribution

In this section, we supplement the velocity field and pressure distribution not provided in §§ 7.2 and 8.2.1, as seen from figures 28–35.

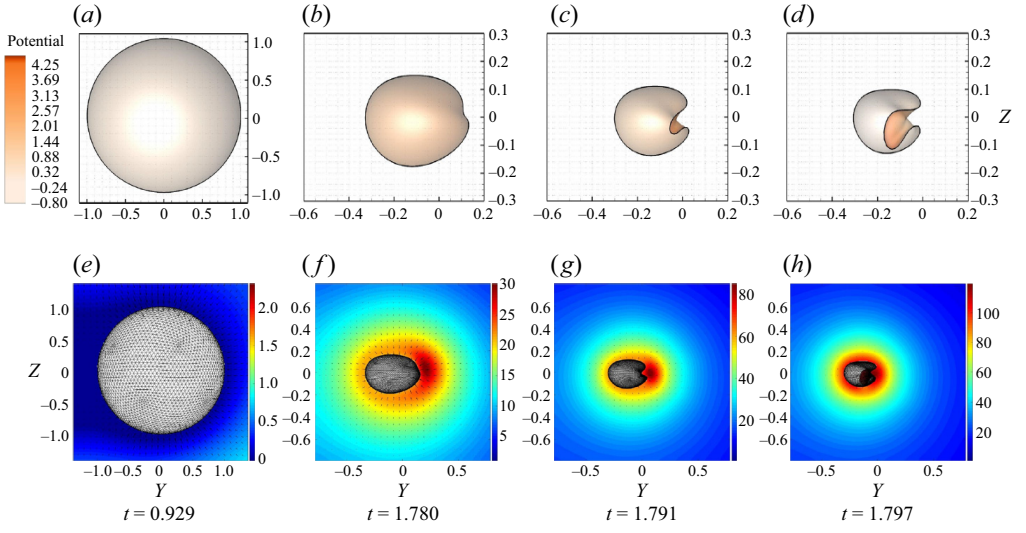

Figure 35. Bubble shape and surrounding pressure distribution at typical moments for $\gamma_f = 2$, $\gamma_w = 3$ and $\delta = 0.239$.

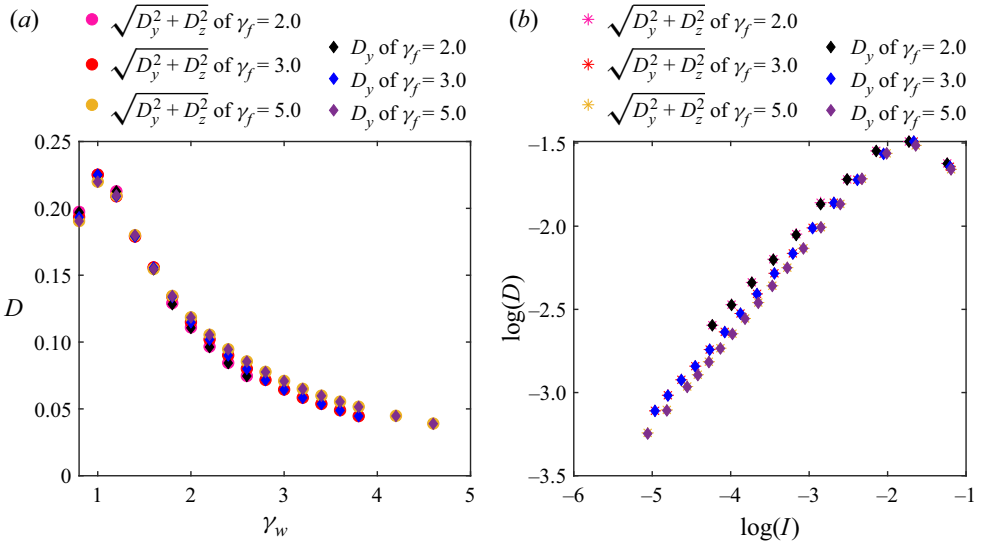

Figure 36. Comparison of the total and horizontal displacement of the bubble at jet impact for different γ_f and γ_w: (*a*) variation in the displacement with γ_w; (*b*) variation in the displacement with theoretical Kelvin impulse I in logarithmic form.

Appendix C. Variation in the total displacement in the 'horizontal jet' pattern

In this section, we give the variation in the total bubble displacement D ($D = \sqrt{D_y^2 + D_z^2}$) with γ_w and the total Kelvin impulse I in the 'horizontal jet' pattern for three γ_f, as shown in figure 36. The change law of D with γ_w is consistent with D_y with negligible differences, so the vertical displacement of the bubble does not change the variation in the bubble displacement or the associated power law.

References

Andrews, E., Rivas, D.F. & Peters, I.R. 2020 Cavity collapse near slot geometries. *J. Fluid Mech.* **901**, A29.

Babak, K. & Martin, L. 2018 Acoustically induced cavity cloud generated by air-gun arrays-comparing video recordings and acoustic data to modeling. *J. Acoust. Soc. Am.* **143** (6), 3383.

Best, J.P. & Blake, J.R. 1994 An estimate of the Kelvin impulse of a transient cavity. *J. Fluid Mech.* **261**, 75–93.

Blake, J.R. 1981 Growth and collapse of a vapour cavity near a free surface. *J. Fluid Mech.* **111**, 123–140.

Blake, J.R. & Gibson, D.C. 1987 Cavitation bubbles near boundaries. *Annu. Rev. Fluid Mech.* **19**, 99–123.

Blake, J.R., Leppinen, D.M. & Wang, Q. 2015 Cavitation and bubble dynamics: the Kelvin impulse and its applications. *Interface Focus* **5** (5), 20150017.

Blake, J.R., Taib, B.M. & Doherty, G. 1986 Transient cavities near boundaries. Part 1. Rigid boundary. *J. Fluid Mech.* **170**, 479–497.

Blake, J.R., Taib, B.M. & Doherty, G. 1987 Transient cavities near boundaries. Part 2. Free surface. *J. Fluid Mech.* **181**, 197–212.

Borkent, B.M., Arora, M., Ohl, C.-D., De Jong, N., Versluis, M., Lohse, D., Mørch, K.A., Klaseboer, E. & Khoo, B.C. 2008 The acceleration of solid particles subjected to cavitation nucleation. *J. Fluid Mech.* **610**, 157–182.

Brujan, E.-A., Hiroyuki, T. & Toshiyuki, O. 2019 Planar jets in collapsing cavitation bubbles. *Exp. Therm. Fluid Sci.* **101**, 48–61.

Brujan, E.-A., Noda, T., Ishigami, A., Ogasawara, T. & Takahira, H. 2018 Dynamics of laser-induced cavitation bubbles near two perpendicular rigid walls. *J. Fluid Mech.* **841**, 28–49.

Brujan, E.-A., Pearson, A. & Blake, J.R. 2005 Pulsating, buoyant bubbles close to a rigid boundary and near the null final Kelvin impulse state. *Intl J. Multiphase Flow* **31** (3), 302–317.

Brujan, E.-A., Zhang, A.-M., Liu, Y.-L., Ogasawara, T. & Takahira, H. 2022 Jetting and migration of a laser-induced cavitation bubble in a rectangular channel. *J. Fluid Mech.* **948**, A6.

Chahine, G. 1977 Interaction between an oscillating bubble and a free surface. *Trans. ASME J. Fluids Engng* **99**, 709–716.

Chahine, G.L., Kapahi, A., Choi, J.K. & Hsiao, C.T. 2016 Modeling of surface cleaning by cavitation bubble dynamics and collapse. *Ultrason. Sonochem.* **29**, 528–49.

Gong, S.W., Ohl, S.-W., Klaseboer, E. & Khoo, B.C. 2018 Interaction of a spark-generated bubble with a two-layered composite beam. *J. Fluids Struct.* **76**, 336–348.

Gonzalez-Avila, S.R., Evert, K., Boo Cheong, K. & Claus-Dieter, O. 2011 Cavitation bubble dynamics in a liquid gap of variable height. *J. Fluid Mech.* **682**, 241–260.

Gregorcic, P., Petkovsek, R. & Mozina, J. 2007 Investigation of a cavitation bubble between a rigid boundary and a free surface. *J. Appl. Phys.* **102**, 094904.

Han, R., Zhang, A.-M., Tan, S. & Li, S. 2022 Interaction of cavitation bubbles with the interface of two immiscible fluids on multiple time scales. *J. Fluid Mech.* **932**, A8.

Javier, C., Galuska, M., Papa, M., LeBlanc, J., Matos, H. & Shukla, A. 2021 Underwater explosive bubble interaction with an adjacent submerged structure. *J. Fluids Struct.* **100**, 103189.

Khodabandeloo, B. & Landro, M. 2018 Acoustically induced cavity cloud generated by air-gun arrays-comparing video recordings and acoustic data to modeling. *J. Acoust. Soc. Am.* **143** (6), 3383.

Kiyama, A., Shimazaki, T., Gordillo, J.M. & Tagawa, Y. 2021 Direction of the microjet produced by the collapse of a cavitation bubble located in a corner of a wall and a free surface. *Phys. Rev. Fluids* **6** (8), 083601.

Klaseboer, E., Hung, K.C., Wang, C., Wang, C.W., Khoo, B.C., Boyce, P., Debono, S. & Charlier, H. 2005*a* Experimental and numerical investigation of the dynamics of an underwater explosion bubble near a resilient/rigid structure. *J. Fluid Mech.* **537** (1), 387–413.

Klaseboer, E., Khoo, B.C. & Hung, K.C. 2005*b* Dynamics of an oscillating bubble near a floating structure. *J. Fluids Struct.* **21** (4), 395–412.

Lauterborn, W. 1982 Cavitation bubble dynamics – new tools for an intricate problem. In *Mechanics and Physics of Bubbles in Liquids: Proceedings IUTAM Symposium, held in Pasadena, California, 15–19 June 1981* (ed. L. Wijngaarden), p. 165–178. Springer.

Lechner, C., Koch, M., Lauterborn, W. & Mettin, R. 2017 Pressure and tension waves from bubble collapse near a solid boundary: a numerical approach. *J. Acoust. Soc. Am.* **142** (6), 3649.

Lechner, C., Lauterborn, W., Koch, M. & Mettin, R. 2019 Fast, thin jets from bubbles expanding and collapsing in extreme vicinity to a solid boundary: a numerical study. *Phys. Rev. Fluids* **4** (2), 021601.

Li, S., Han, R., Zhang, A.-M. & Wang, Q. 2016 Analysis of pressure field generated by a collapsing bubble. *Ocean Engng* **117**, 22–38.

LI, S.-M., LIU, Y.-L., WANG, Q. & ZHANG, A.-M. 2021 Dynamics of a buoyant pulsating bubble near two crossed walls. *Phys. Fluids* **33** (7), 073310.

LI, S.-M., ZHANG, A.-M. & LIU, N.-N. 2021 Effect of a rigid structure on the dynamics of a bubble beneath the free surface. *Theor. App. Mech. Lett.* **11** (6), 100311.

LI, S.-M., ZHANG, A.-M., WANG, Q. & ZHANG, S. 2019*a* The jet characteristics of bubbles near mixed boundaries. *Phys. Fluids* **31** (10), 107105.

LI, T., ZHANG, A.-M., WANG, S.-P., LI, S. & LIU, W.-T. 2019*b* Bubble interactions and bursting behaviors near a free surface. *Phys. Fluids* **31** (4), 042104.

LIU, N.-N., ZHANG, A.-M., CUI, P., WANG, S.-P. & LI, S. 2021 Interaction of two out-of-phase underwater explosion bubbles. *Phys. Fluids* **33**, 106103.

LIU, W.-T., ZHANG, A.-M., MIAO, X.-H., MING, F.-R. & LIU, Y.-L. 2023 Investigation of hydrodynamics of water impact and tail slamming of high-speed water entry with a novel immersed boundary method. *J. Fluid Mech.* **958**, A42.

LIU, Y.-L., WANG, Q., WANG, S.-P. & ZHANG, A.-M. 2016 The motion of a 3D toroidal bubble and its interaction with a free surface near an inclined boundary. *Phys. Fluids* **28** (12), 122101.

LYONS, J.J., HANEY, M.M., FEE, D., WECH, A.G. & WAYTHOMAS, C.F. 2019 Infrasound from giant bubbles during explosive submarine eruptions. *Nat. Geosci.* **12** (11), 952–958.

MENDOZA, J.C., CLEMENTE, S. & HERNANDEZ, J.C. 2020 Modeling the role of marine protected areas on the recovery of shallow rocky reef ecosystem after a catastrophic submarine volcanic eruption. *Mar. Environ. Res.* **155**, 104877.

MOLEFE, L. & PETERS, I.R. 2019 Jet direction in bubble collapse within rectangular and triangular channels. *Phys. Rev.* E **100** (6-1), 063105.

NGUYEN, V.-T., PHAN, T.-H., DUY, T.-N. & PARK, W.-G. 2021 Numerical modeling for compressible two-phase flows and application to near-field underwater explosions. *Comput. Fluids* **215**, 104805.

PHILIPP, A. & LAUTERBORN, W. 1998 Cavitation erosion by single laser – produced bubbles. *J. Fluid Mech.* **361**, 75–116.

PLESSET, M.S. & PROSPERETTI, A. 1977 Bubble dynamics and cavitation. *Annu. Rev. Fluid Mech.* **9** (1), 145–185.

RAYLEIGH, LORD 1917 On the pressure developed in a liquid during the collapse of a spherical cavity. *Phil. Mag*. **34**, 94–98.

SAADE, Y., JALAAL, M., PROSPERETTI, A. & LOHSE, D. 2021 Crown formation from a cavitating bubble close to a free surface. *J. Fluid Mech.* **926**, A5.

SHIMA, A. & SATO, Y. 1980 The behavior of a bubble between narrow parallel plates. *Z. Angew. Math. Phys.* **31**, 692–704.

SHIMA, A., TOMITA, Y., GIBSON, D.C. & BLAKE, J.R. 1989 The growth and collapse of cavitation bubbles near composite surfaces. *J. Fluid Mech.* **203**, 199–214.

SONG, G., CHEN, Z.-Y., LONG, Y., ZHONG, M.-S. & WU, J.-Y. 2017 Experimental and numerical investigation of the centrifugal model for underwater explosion shock wave and bubble pulsation. *Ocean Engng* **142**, 523–531.

SUPPONEN, O., OBRESCHKOW, D., TINGUELY, M., KOBEL, P., DORSAZ, N. & FARHAT, M. 2016 Scaling laws for jets of single cavitation bubbles. *J. Fluid Mech.* **802**, 263–293.

TAGAWA, Y. & PETERS, I.R. 2018 Bubble collapse and jet formation in corner geometries. *Phys. Rev. Fluids* **3** (8), 081601.

TIAN, Z.-L., LIU, Y.-L., ZHANG, A.-M., TAO, L. & CHEN, L. 2020 Jet development and impact load of underwater explosion bubble on solid wall. *Appl. Ocean Res.* **95**, 102013.

TOMITA, Y., KODAMA, T. & SHIMA, A. 1991 Secondary cavitation due to interaction of a collapsing bubble with a rising free surface. *Appl. Phys. Lett.* **59** (3), 274–276.

TOMITA, Y. & SHIMA, A. 1986 Mechanisms of impulsive pressure generation and damage pit formation by bubble collapse. *J. Fluid Mech.* **169**, 535–564.

TURANGAN, C.K., ONG, G.P., KLASEBOER, E. & KHOO, B.C. 2006 Experimental and numerical study of transient bubble-elastic membrane interaction. *J. Appl. Phys.* **100** (5), 054910.

VOGEL, A. & LAUTERBORN, W. 1988 Acoustic transient generation by laser – produced cavitation bubbles near solid boundaries. *J. Acoust. Soc. Am.* **84**, 719.

WANG, Q. 2013 Non-spherical bubble dynamics of underwater explosions in a compressible fluid. *Phys. Fluids* **25** (7), 072104.

WANG, Q. & BLAKE, J.R. 2010 Non-spherical bubble dynamics in a compressible liquid. Part 1. Travelling acoustic wave. *J. Fluid Mech.* **659**, 191–224.

WANG, Q. & BLAKE, J.R. 2011 Non-spherical bubble dynamics in a compressible liquid. Part 2. Acoustic standing wave. *J. Fluid Mech.* **679**, 559–581.

WANG, Q., KAWA, M. & MICHAEL, C. 2015 Numerical modeling of the 3D dynamics of ultrasound contrast agent microbubbles using the boundary integral method. *Phys. Fluids* **27** (2), 022104.

WANG, Q., YEO, K.S., KHOO, B.C. & LAM, K.Y. 1996*a* Nonlinear interaction between gas bubble and free surface. *Comput. Fluids* **25** (7), 607–628.

WANG, Q., YEO, K.S., KHOO, B.C. & LAM, K.Y. 1996*b* Strong interaction between a buoyancy bubble and a free surface. *Theor. Comput. Fluid Dyn.* **8**, 73–88.

WU, S., ZUO, Z., STONE, H.A. & LIU, S. 2017 Motion of a free-settling spherical particle driven by a laser-induced bubble. *Phys. Rev. Lett.* **119** (8), 084501.

ZHANG, A.-M., CUI, P., CUI, J. & WANG, Q. 2015 Experimental study on bubble dynamics subject to buoyancy. *J. Fluid Mech.* **776**, 137–160.

ZHANG, A.-M., LI, S.-M., CUI, P., LI, S. & LIU, Y.-L. 2023*a* A unified theory for bubble dynamics. *Phys. Fluids* **35** (3), 033323.

ZHANG, A.-M., LI, S.-M., CUI, P., LI, S. & LIU, Y.-L. 2023*b* Interactions between a central bubble and a surrounding bubble cluster. *Theor. Appl. Mech. Lett.*, 100438.

ZHANG, A.-M. & LIU, Y.-L. 2015 Improved three-dimensional bubble dynamics model based on boundary element method. *J. Comput. Phys.* **294**, 208–223.

ZHANG, N. & ZONG, Z. 2011 The effect of rigid-body motions on the whipping response of a ship hull subjected to an underwater bubble. *J. Fluids Struct.* **27** (8), 1326–1336.

ZHANG, N., ZONG, Z. & ZHANG, W. 2014 Dynamic response of a surface ship structure subjected to an underwater explosion bubble. *Mar. Struct.* **35**, 26–44.

ZHANG, S., ZHANG, A.-M., WANG, S.-P. & CUI, J. 2017 Dynamic characteristics of large scale spark bubbles close to different boundaries. *Phys. Fluids* **29** (9), 092107.

ZHANG, Y., XIE, X., ZHANG, Y., ZHANG, Y. & DU, X. 2019 Experimental study of influences of a particle on the collapsing dynamics of a laser-induced cavitation bubble near a solid wall. *Exp. Therm. Fluid Sci.* **105**, 289–306.

ZHANG, Y.L., YEO, K.S., KHOO, B.C. & WANG, C. 2001 3D jet impact and toroidal bubbles. *J. Comput. Phys.* **166** (2), 336–360.

ZIOLKOWSKI, A., PARKES, G., HATTON, L. & HAUGLAND, T. 1982 The signature of an air gun array: computation from near-field measurements including interactions. *Geophysics* **47** (10), 1413–1421.

ZIOLKOWSKI, A. 2021 Inversion of explosive source land seismic data to determine source signature parameters. *Geophys. Prospect.* **69** (4), 679–708.

ZONG, Z., WANG, J.-X., ZHOU, L. & ZHANG, G.-Y. 2015 Fully nonlinear 3D interaction of bubble dynamics and a submerged or floating structure. *Appl. Ocean Res.* **53**, 236–249.